Colloids and Surfaces B: Biointerfaces 267 (2026) 115967

Contents lists available at ScienceDirect

Colloids and Surfaces B: Biointerfaces

journal homepage: www.elsevier.com/locate/colsurfb

Size-dependent interfacial retention of vaterite particles under tear flow: Linking hydrodynamic detachment to ocular pharmacodynamics

A.V. Mikheev [a], E.V. Popova [b], O.V. Beznos [c], O.A. Kost [b], C. Zhu [e], X.Z. Chen [d,f], I.A. Kasyanov [b], I.A. Burmistrov [a], V.V. Artemov [a], T.N. Pallaeva [a], T.V. Bukreeva [a], A.A. Abalymov [d,*], D.B. Trushina [a,*]

[a] A. V. Shubnikov Institute of Crystallography of the Kurchatov Complex Crystallography and Photonicsof the NRC "Kurchatov Institute", Moscow 119333, Russia
[b] Faculty of Chemistry, Lomonosov Moscow State University, Moscow 119991, Russia
[c] Helmholtz National Medical Research Center of Eye Diseases, Moscow 105062, Russia
[d] International Institute for Intelligent Nanorobots and Nanosystems & State Key Laboratory of Surface Physics, College of Intelligent Robotics and Advanced Manufacturing, Fudan University, Shanghai 200438, People's Republic of China
[e] School of Basic Medical Sciences, State Key Laboratory of Brain Function and Disorders, Fudan University, Shanghai 200438, China
[f] Zhejiang Key Laboratory of Extreme Environment Functional Materials, Yiwu Research Institute of Fudan University, Yiwu 322000, Zhejiang, People's Republic of China

ARTICLE INFO

Keywords:
Vaterite particles
Mucoadhesion
Size-dependent interfacial retention
Ocular drug delivery
Intraocular pressure
Enalaprilat

ABSTRACT

Rapid precorneal clearance remains a major limitation of topical ocular therapy, yet the fundamental physical mechanisms governing particle retention under tear flow are poorly understood. Current delivery strategies primarily rely on empirical optimization of surface chemistry, while the role of particle size in interfacial stability under dynamic conditions remains largely unexplored. Here, we establish a mechanistic size-retention-pharmacodynamic framework for porous vaterite particles designed as mucoadhesive ocular drug carriers. Two structurally equivalent particle fractions were engineered: micron-sized (3.8 ± 0.5 μm) and submicron (0.65 ± 0.15 μm) particles with preserved vaterite phase stability in simulated tear fluid, porous architecture, comparable surface physicochemical properties, matched enalaprilat loading (~5 wt%), and diffusion-controlled release kinetics. This design enabled isolation of particle size as the primary variable governing interfacial behavior. Under tear-mimicking flow on mucin-coated substrates, submicron particles exhibited ~1.8-fold slower washout compared to micron-sized counterparts. This difference is consistent with a size-dependent balance between hydrodynamic torque and adhesive stabilization, where detachment propensity increases with particle diameter. Ex vivo corneal experiments under ~100 × accelerated physiological tear flow revealed convergence of retention (~10% surface coverage after 2 h), indicating a transition from physics-dominated to biology-dominated interfacial behavior on native tissue. Most importantly, these interfacial effects were associated with improved therapeutic performance *in vivo*. Submicron enalaprilat-loaded particles produced a more sustained intraocular pressure reduction and an approximately 2.1-fold increase in cumulative intraocular pressure-lowering effect compared to free drug, whereas micron-sized particles showed no clear improvement. Developed formulations demonstrated good cytocompatibility and excellent ocular tolerability in vitro and in vivo. Overall, this work identifies particle size as a key parameter of interfacial retention under flow and suggests that reducing hydrodynamic detachment at mucosal interfaces can enhance ocular pharmacodynamic performance without increasing the administered drug dose. The presented framework provides a basis for rational design of interface-controlled drug delivery systems beyond empirical formulation approaches.

1. Introduction

Rapid clearance at biological interfaces remains one of the most fundamental limitations of topical drug delivery, particularly at the ocular surface, where tear turnover, blinking, and fluid drainage remove the majority of administered formulations within seconds. Despite decades of research, most strategies aimed at improving ocular bioavailability rely on empirical optimization of formulation properties - such as

* Corresponding authors.
E-mail addresses: anatolii_abalymov@fudan.edu.cn (A.A. Abalymov), trushina.d@mail.ru (D.B. Trushina).

https://doi.org/10.1016/j.colsurfb.2026.115967
Received 1 April 2026; Received in revised form 8 June 2026; Accepted 5 July 2026
Available online 11 July 2026
0927-7765/© 2026 Elsevier B.V. All rights are reserved, including those for text and data mining, AI training, and similar technologies.

viscosity, surface charge, or polymer-mediated mucoadhesion - without addressing the underlying physical mechanisms governing particle retention under flow. In reality, retention at mucosal interfaces emerges from a dynamic balance between hydrodynamic forces that promote detachment and interfacial interactions that stabilize particles at the surface. However, this balance remains poorly quantified, and the role of particle size as a governing parameter in this process has not been systematically established.

High intraocular pressure (IOP) remains the primary modifiable risk factor for glaucoma, a leading cause of irreversible blindness worldwide [1,2]. Effective IOP reduction typically requires long-term topical therapy, however, conventional eye drops suffer from rapid precorneal clearance driven by tear turnover, blinking, and nasolacrimal drainage, resulting in poor bioavailability. Most instilled formulations are cleared within 15–30 s, and less than 4–5% of the administered dose reaches the anterior chamber [3–5], necessitating frequent dosing and limiting therapeutic efficiency. Colloidal delivery systems emerged as a promising strategy to enhance ocular bioavailability [6–8]. Both inorganic [9–13] and polymer [14–18] carriers demonstrated improved pharmacodynamic performance of IOP-lowering agents, including angiotensin-converting enzyme (ACE) inhibitors, β-blockers, and carbonic anhydrase inhibitors. Calcium phosphate nanoparticles (40–300 nm), for example, enabled approximately two-fold enhancement in IOP reduction for lisinopril, enalaprilat, and timolol compared to free drugs [19–22], with further improvement achieved via chitosan modification [9,22,23]. Another formulation of calcium phosphate nanoparticles (200 – 300 nm) loaded with methazolamide demonstrated a six-fold greater efficacy in IOP reduction and prolongation of the therapeutic effect by 2.5 times compared to the administration of the free drug [12].

Despite these advances, current approaches remain largely guided by formulation optimization - such as surface functionalization or rheological tuning - while the mechanistic role of particle size in governing interfacial retention under dynamic tear flow remains insufficiently quantified. In most systems, particle size is intrinsically coupled with variations in composition, porosity, or surface chemistry, making it difficult to isolate purely geometric effects. As a result, a systematic size-retention-efficacy relationship linking interfacial washout kinetics to *in vivo* pharmacodynamic outcome has not been established.

Among inorganic carriers, the vaterite polymorph of $CaCO_3$ provides a suitable model platform for addressing this limitation due to its tunable polycrystalline porous architecture and well-established synthesis routes that enable precise control over particle size and morphology [24–27]. In addition, vaterite exhibits high affinity for ocular mucins (up to ~16 wt% adsorption [28]), which not only enhances mucoadhesion but also stabilizes the vaterite phase against recrystallization, preserving diffusion-controlled release behavior. These features make size-controlled vaterite particles particularly well suited for isolating particle diameter as an independent design parameter in interfacial studies.

Enalaprilat (ENL), an FDA-approved angiotensin-converting enzyme (ACE) inhibitor, was selected as a clinically relevant model drug for IOP reduction [29]. In comparative preclinical studies, ENL demonstrated one of the most pronounced and sustained ocular hypotensive effects among ACE inhibitors [30–32]. Its efficacy has also been enhanced in particulate delivery systems [9,22], supporting its suitability for evaluating interface-controlled topical formulations. Its small molecular size and hydrophilic character enable clear assessment of diffusion-controlled release from porous inorganic matrices, making it an appropriate probe for evaluating interface-controlled delivery.

In this work, we engineer two structurally equivalent porous vaterite fractions differing only in diameter to isolate particle size as the governing variable of interfacial behavior. By combining controlled shear flow experiments on mucin-coated substrates, *ex vivo* corneal models, and *in vivo* pharmacodynamic evaluation of enalaprilat, we establish a size-retention-pharmacodynamic framework connecting dynamic interfacial retention with the magnitude and duration of IOP reduction.

2. Materials and Methods

2.1. Materials

The sources of the chemicals are as follows: $CaCl_2$ (99%), Na_2CO_3 (99%), ethylene glycol (PanReac AppliChem, Spain); NaOH (99%), mucin from porcine stomach (type II), lysozyme from chicken egg white, phosphate saline buffer (PBS), 4-(2-hydroxyethyl)piperazine−1-ethane sulfonic acid (HEPES), ethylenediaminetetraacetic acid disodium salt (EDTA), glutaraldehyde, ethanol, fluorescein isothiocyanate–labeled dextran (FITC-dextran, MW 20 kDa), Bradford Reagent, K_2HPO_4, HCl, H_2O_2 (all Sigma-Aldrich, Germany); oxybuprocaine, bovine serum albumin (BSA, MW 68 kDa) (DIA-M, Russia), NaCl (Gematek, Russia), enalaprilat ((2S)−1-[(2S)−2-{[(1S)−1-carboxy−3-phenylpropyl] amino}propanoyl]pyrrolidine−2-carboxylic acid) (U.S. Pharmacopeial Convention, Rockville, MD, USA) and benzyloxycarbonyl-L-phenylalanyl-L-histidyl-L-leucine (Cbz-Phe-His-Leu, Bachem AG, Switzerland). Angiotensin-converting enzyme (ACE) was purified from bovine lung using affinity chromatography on lisinopril–Sepharose [33]. HLEpiC and HCE-T cell lines, DMEM, DMEM/F12, 20% Fetal Bovine Serum (FBS), penicillin/streptomycin, insulin, trypsin, epidermal growth factor, CellTrace™ Calcein Red-Orange and Hoechst 34580 were purchased from Thermo Fisher Scientific (USA), CCK−8 was purchased from Dojindo (Japan). Deionized water from a three-stage Milli-Q Plus purification system was used in the experiments.

2.2. Vaterite Particle Synthesis and Loading

2.2.1. Synthesis of Size-Controlled Vaterite Particles

Micron-sized vaterite particles (M-Vat) were synthesized according to Volodkin et al. [34], whereas submicron vaterite particles (SM-Vat) were prepared using the ethylene glycol-assisted synthesis described previously [35]. For M-Vat synthesis, equal volumes (2 mL) of 0.33 M $CaCl_2$ and 0.33 M Na_2CO_3 were mixed using magnetic stirrer (500 rpm) for 60 s. The resulting suspension was centrifuged at 5000 rpm for 5 min (Eppendorf MiniSpin plus, Eppendorf AG, Germany), and the precipitated particles were washed 3 times with water. For SM-Vat synthesis, 500 μL of 0.5 M $CaCl_2$ and 500 μL 0.5 M Na_2CO_3 were added to 5 mL of ethylene glycol under stirring at 500 rpm. The mixture was stirred for 1 h, and then centrifuged at 14500 rpm for 15 min (Eppendorf MiniSpin plus, Eppendorf AG, Germany). The precipitates were subjected to three washes with water. The obtained particles were dried at 90°C and stored at room temperature.

2.2.2. Drug Loading and Model Fluorescent Labeling

ENL loading into M-Vat and SM-Vat was performed using the freezing-induced loading method [36]. For this, 2 mL of an aqueous ENL solution (2 mg/mL) was added to the dried particle samples. Because M-Vat and SM-Vat differ in porous architecture and accessible pore volume, the particle-to-drug mass ratios were adjusted to obtain comparable final ENL loading capacities rather than identical initial loading conditions: 25:4 for M-Vat:ENL and 8:4 for SM-Vat:ENL. The mixtures were sonicated for 5 min at 80 W and 37 kHz (Elmasonic S10H, Elma, Germany), after which the tubes were placed on a rotator and frozen at −20°C for 2 h. Following thawing at room temperature, the suspensions were centrifuged, and the precipitates were washed with water. The resulting ENL-loaded micron-sized vaterite particles (M-Vat/ENL) and ENL-loaded submicron vaterite particles (SM-Vat/ENL) were lyophilized (FreeZone 12, Labconco, Kansas, USA) and stored 5°C.

FITC-dextran labeled M-Vat and SM-Vat were prepared by coprecipitation [37]. To obtain labeled M-Vat, 615 μL of 1 M $CaCl_2$ and 615 μL of 1 M Na_2CO_3 were added to 2.5 mL of FITC-dextran solution (2 mg/mL). The mixture was stirred on a magnetic stirrer at 500 rpm for 60 s, followed by centrifugation. The resulting precipitate was

thoroughly washed with water, lyophilized, and stored in the dark at room temperature. For FITC-dextran–labeled SM-Vat, 600 μL of FITC-dextran solution (2 mg/mL), 200 μL of 1 M $CaCl_2$, and 200 μL of 1 M Na_2CO_3 were sequentially added to 5 mL of ethylene glycol under stirring (500 rpm). After 1 h, the suspension was centrifuged, and the precipitate was thoroughly washed and lyophilized. The particles were stored at room temperature in the dark.

To determine ENL loading, 1 mg of M-Vat/ENL and SM-Vat/ENL were incubated in 500 μL of 1 mM HCl until complete particles dissolution. The resulting amount of ENL in the particles was evaluated indirectly by its ability to inhibit the activity of the control the ACE. ACE activity was determined fluorimetrically with 0.2 MM Cbz-Phe-His-Leu as a substrate [38] in 0.15 M HEPES, pH 7.5, containing 0.15 M NaCl, 1 μM $ZnCl_2$, at 25 °C on an Infinite M−200 reader (Tecan, Austria). Preliminarily, the calibration curve of the dependence of the residual ACE activity on the concentration of control ENL (0.01 – 100 nM) was obtained and the value of IC50 was determined. Then, the curves of residual ACE activity on the dilution of ENL solution after particles dissolution were plotted. The dilution at which ACE activity was equal to half maximum was found by the graph. The concentration of ENL at this dilution was considered to be IC50. The dilution value was used to recalculate the initial concentration of ENL in the sample. Encapsulation efficiency (EE) and loading capacity (LC) were determined as follows:

$$EE(\%) = \frac{\text{Mass of encapsulated drug}}{\text{Mass of drug added}} * 100\%, \quad (1)$$

$$LC(\%) = \frac{\text{Mass of encapsulated drug}}{\text{Mass of vaterite particles}} * 100\%, \quad (2)$$

.

2.3. Physicochemical Characterization of Vaterite Particles

The morphology and size of particles were analyzed using scanning electron microscopy (SEM) (JSM-7401F, JEOL, Japan) operated at 1 kV. The particle sizes were determined by ImageJ software.

The hydrodynamic diameter and zeta potential were investigated at 25 °C using dynamic and electrophoretic light scattering (Zetasizer Nano ZS, Malvern Panalytical Ltd., Malvern, UK).

Powder X-ray diffractometry (XRD) were used to study structure of the obtained particles. The X-ray diffraction patterns were measured using a Rigaku Miniflex 600 diffractometer (Rigaku Corp., Japan) with CuK_α radiation ($\lambda = 1.5418$ Å). Samples were scanned at a Bragg angle 2θ from 10 to 90 ° and a step size of 0.02 ° at room temperature. The phase composition was determined by a Rietveld full-pattern-fitting method using Xpert HighScore software. The average size of the coherent scattering regions was estimated using the Scherrer formula, assuming their spherical shape and taking the constant $K = 0.9$.

To evaluate structural stability under physiological conditions, the particles were incubated in simulated tear fluid (STF). STF was prepared as previously described in [39] by dissolving 9.5 mg lysozyme, 1 mg BSA and 0.75 mg mucin in 5 mL of 0.01 M PBS. M-Vat and SM-Vat particles (30 mg) were incubated in 2 mL of STF for 6 h (concentration was selected to match the particle dose used later in the *in vivo* ocular instillation experiments). The samples were washed 3 times with water, freeze-dried, analyzed by XRD, and the phase composition of particles incubated in STF was determined in the same manner as for intact particles.

The analysis of porous structure was carried out on an automatic sorbtometer ASAP 2020 (Micromeritics, USA). Prior to measurement, the samples were degassed (30 °C, 8 h). Brunauer–Emmett–Teller (BET) theory and the Barrett–Joyner–Halenda model with Harkins and Jura equation were used for surface area and pore-size distribution analysis, respectively.

ENL release studies were performed using a complete medium replacement design. M-Vat/ENL and SM-Vat/ENL (1 mg) were resuspended in 500 μL of saline (pH 7.5) and incubated for 5 – 120 min at room temperature. This concentration was sufficient for accurate ACE-based quantification while maintaining sink conditions. Given the ENL loading of ~5 wt% (≈50 μg ENL per mg of particles), the maximal theoretical concentration of ENL remained well below its aqueous solubility (0.876 mg/mL [40]). At each time point, the entire 500 μL supernatant was collected after centrifugation (5 min, 5400 g), diluted 3-fold, and the concentration of the ENL was analyzed via ACE inhibition. Each time point was measured on an independent particle sample to maintain sink conditions and prevent accumulation of released drug. At least three experiments were conducted to determine the kinetics of desorption of ENL from the particles. The mathematical analysis of experimental kinetic curves *in vitro* was carried out using well-known mathematical models (first order, Higuchi, Hixson-Crowell, Korsmeyer-Peppas) describing the release of drugs from matrices of various chemical nature [22].

2.4. In vitro Studies

2.4.1. Preparation of Mucin-Coated Substrates

Glass slides coated with mucin were used as simplified mucoadhesion test platforms to evaluate particle retention under STF. Following a previously established protocol [41] glass slides were cleaned and then incubated for 2 h in 5 wt% aqueous solution of porcine gastric mucin (pH 4.0) under constant stirring to ensure uniform polymer film formation. The coating was air-dried, and the adsorption/drying cycle was repeated twice to enhance surface coverage. Successful mucin immobilization was confirmed gravimetrically after each adsorption/drying stage and by protein staining using Bradford reagent, with UV/vis detection at 595 nm (Lambda C650, PerkinElmer, USA).

2.4.2. Contact Angle Measurements

The wettability of particle suspensions was evaluated by measuring the contact angle of sessile drops on uncoated and mucin-coated glass substrates following the established protocol [42]. Three sample types were investigated: PBS, and suspensions of M-Vat and SM-Vat in PBS at a concentration of 16 mg/mL, corresponding to that used in the *in vivo* experiments. For each measurement, a 5 μL droplet of the corresponding liquid or suspension was carefully placed onto the substrate surface using a calibrated micropipette. The droplets were imaged using a digital microscope (Andonstar AD 208S, Andonstar Co., Ltd., China) positioned laterally relative to the substrate plane to ensure accurate visualization of the droplet profile. High-resolution side-view images were analyzed using ImageJ software to determine the angle at the liquid–solid–air interface (contact angle, θ). The data were analyzed to determine the difference in wettability among the suspensions and, in addition, served as an indirect verification of successful mucin layer formation, confirming the modification of the glass surface with a hydrophilic glycoprotein film.

2.4.3. Surface Tension Measurements

Surface tension measurements were included to confirm that the particle suspensions retained liquid-like behavior and water-like interfacial properties at the selected concentration of 16 mg/mL in PBS, ensuring their suitability for drop formation and ocular application. The surface tension of particle suspensions (γ) was determined using the pendant drop method. Droplets were generated at the tip of a stainless-steel capillary with an outer diameter of 0.9 mm, and each drop had a volume of ~5 μL. The droplet formation process was recorded at room temperature using a digital camera (GP-300C, KSGAOPIN, China) (1.5 × optical magnification, 60 frames/s). The recorded data analyzed using ImageJ equipped with the Pendant Drop plugin [43]. Each frame was processed to extract the droplet profile, and the surface tension was calculated from the equilibrium drop shape based on the Young–Laplace equation. At least ten independent droplets were analyzed for each

sample, and the results are reported as mean ± standard deviation. Work of adhesion (W_a) was calculated from the measured surface tension γ and contact angle θ values according to the Young–Dupré relationship:

$$W_a = \gamma(1 + \cos\theta) \quad (3)$$

.

2.4.4. In Vitro Mucoadhesive Retention Under Flow

Suspensions of FITC-dextran labeled M-Vat and SM-Vat (25 μL, 8.6 mg/mL) were applied to both mucin-coated and uncoated glass slides. Uncoated glass slides were used in parallel as controls to differentiate mucoadhesion-driven retention from nonspecific surface interactions. Mucoadhesive performance was assessed using rinsing experiments and the inclined plane method under dynamic conditions consistent with standard protocol frequently employed in microparticle mucoadhesion assays [44,45]. For this, slides were mounted at a 30 ° incline and subjected to continuous rinsing with STF using a syringe pump (SinoMDT, China) at a constant flow rate of 10 mL/min. This flow rate exceeds the physiological tear turnover by approximately 5000–10000-fold and was therefore used as an accelerated clearance stress test rather than as a direct simulation of basal tear flow, providing stringent conditions to challenge particle adhesion and compare retention between particle fractions.

Confocal fluorescence microscopy (Leica TCS SP, Leica Microsystems, Germany) was used to visualize particle coverage before and after rinsing under identical imaging conditions. To quantify particle removal, the relative mass of retained fluorescently labeled particles was determined by measuring the decrease in fluorescence intensity using calibration curves (Figure S6). For each particle type, five independent experiments were conducted, data are represented as a mean value ± standard deviation. The fraction of particles remaining on the surface over time was fitted with an exponential decay model:

$$\frac{M_t}{M_0} = e^{-kt}, \quad (4)$$

.

where M_0 and M_t are the initial particle mass and the mass retained at time t, respectively, and k is the washout rate constant (h^{-1}) characterizing particle detachment kinetics under flow.

2.4.5. Cell Cultivation and Spheroid Formation

For biocompatibility assessment, two ocular cell lines were employed. Human lens epithelial cells (HLEpiC) were selected as a sensitive model for preliminary toxicity evaluation because of their essential role in maintaining lens transparency and ocular homeostasis. Human corneal epithelial cells (HCE-T) were used as a physiologically relevant model representing the primary site of contact for topical ocular formulations. HLEpiC were cultured in DMEM supplemented with 20% FBS and 1% penicillin/streptomycin. HCE-T were cultured in DMEM/F12 medium supplemented with 5% FBS, insulin (5 μg/mL), epidermal growth factor (10 ng/mL), and 1% penicillin/streptomycin. The medium was replaced every 3 days, and the cells were maintained in a humidified incubator at 5% CO_2 and 37 °C (Innova CO−170, New Brunswick Scientific, Edison, NJ, USA). Cellular spheroids were formed from HLEpiC cells using ultra-low adhesion Corning spheroid microplates (Corning, Cat. #4520, USA) following the manufacturer's protocol. Briefly, monolayer cells at 95% confluence were rinsed with PBS, harvested from culture flasks using 0.25% trypsin/0.53 mM EDTA, and suspended in cell culture medium at a concentration of 2×10^5 cells/mL. A 10 μL volume of the cell suspension was dispensed into the wells of Corning spheroid microplates, followed by the addition of 90 μL of culture medium. The microplates were incubated at 37 °C in a humidified atmosphere with 5% CO_2 for 3 days.

2.4.6. Cellular Uptake Analysis

Fluorescence microscopy was employed to visualize particles uptake into the single cells and spheroids. For this HLEpiC single cells and spheroids were co-incubated with particles (10, 50, and 100 μg/well, which corresponds to the particle mass/area ratio, which is used for *in vivo* experiments) for 24 h in 37 °C in CO_2 incubator. Single cells and spheroids were stained with CellTrace™ Calcein Red-Orange and Hoechst 34580. For staining, 2 μM of the dyes was added to the culture medium. The cells were incubated at for 15 min, then washed with PBS for three times, and fresh medium was added. Fluorescent images were acquired using a fluorescence microscope (Nikon Eclipse Ti, Nikon Instruments, Japan) with 10 ×, 20 ×, and 60 × objectives and appropriate filters. To obtain z-stacks, 30 images were captured along the z-axis with 0.3 μm intervals. Fluorescent intensity profiles were extracted from three different spheroid and analyzed using ImageJ and OriginLab software.

To confirm particle adhesion and penetration, spheroids were fixed in 2.5% glutaraldehyde, placed on a stub, dehydrated, sputter-coated with gold (Leica EM ACE 600 Sputter Coater, Leica Microsystems, Buffalo Grove, IL, USA), and imaged using a field-emission scanning electron microscope at 3 keV (FEI Quanta 400 ESEM FEG, FEI, Hillsboro, OR, USA).

2.4.7. Cytocompatibility Assessment

Cell Viability Assay (CCK−8) was performed to evaluate cell viability after co-incubation with FITC-dextran labeled vaterite particles. HLEpiC cells were seeded in 96-well plates at a density of 1×10^4 cells per well and allowed to adhere for 24 h. Than M-Vat, SM-Vat, M-Vat/ENL and SM-Vat/ENL were added to wells at concentrations of 10, 50, and 100 μg/well, which corresponds to the particle mass/area ratio, which is used for *in vivo* experiments, and incubated for additional for 24 h. After incubation, 10 μL of the CCK−8 reagent was added to each well, followed by incubation at 37 °C for 2 h. Absorbance was measured at 450 nm using a microplate reader (BioTek, USA). Cell viability was calculated as a percentage relative to the untreated control group. The assay was repeated in triplicate, and results were presented as mean ± standard deviation.

2.4.8. Hemocompatibility Assessment

The erythrocyte-compatibility of particles was evaluated using a rabbit red blood cell assay according to a previous study [46]. Briefly, fresh rabbit blood (2 mL) was collected into a tube prefilled with 3.8% sodium citrate solution as an anticoagulant. The sample was centrifuged at 5000 rpm for 5 min, erythrocytes were collected and washed three times with PBS (3 mL, pH 7.4), and then diluted 1:10 in PBS. For each measurement, 100 μL of the 10% (w/v) erythrocytes suspension was mixed with 900 μL of particle PBS suspensions at concentrations ranging from 0.0001 to 0.1 mg/mL. Samples were incubated at 37 °C for 1 h on a shaker (100 rpm). The ratio of erythrocytes to particles was selected to ensure that the particles did not cause alkalinization of the closed system; however, after 1 h of incubation, a slight increase from pH 7.4–7.9 was observed. Following incubation, samples were centrifuged at 5000 rpm for 5 min, and the absorbance of the supernatant was measured at 415 nm using a microplate reader (Infinite 500, TECAN, Switzerland). The hemolysis rate (HR) was calculated according to:

$$HR(\%) = \frac{A_s - A_{PBS}}{A_{Triton} - A_{PBS}} * 100\% \quad (5)$$

.

Where A_s is the absorbance of the experimental sample, A_{PBS} (negative control) represents 0% erythrocyte lysis, and A_{Triton} (10% Triton X−100, positive control) represents 100% erythrocyte lysis. Data are presented as mean ± standard deviation (n = 3).

2.5. Ex vivo Corneal Retention Study

To evaluate the retention of particles on the ocular surface under simulated lacrimation, an *ex vivo* corneal model was employed. Following previously reported methodologies [47,48], fresh rabbit eyes were obtained within 3 h post-mortem, corneas were carefully dissected, rinsed with a freshly prepared STF and mounted on microscope glass slides with the outer epithelial side facing upward. A 50 μL droplet of a suspension of FITC-dextran labeled particles was applied to the center of the corneal surface. The applied concentration corresponded to the therapeutic dose of particles loaded with ENL in experiments *in vivo*. After 2 min, the corneal samples were positioned at a 30 ° inclination angle, and a continuous simulated tear flow at 100 μL/min was applied over the corneal surface using a syringe pump (SinoMDT, China). This flow rate exceeds baseline unstimulated human tear flow (1–2 μL/min) and the reported range of stimulated tear secretion, up to approximately 50 μL/min [49,50]. Thus, the *ex vivo* assay should be considered a conservative accelerated lacrimation model rather than a direct simulation of basal tear turnover. The selected flow rate enabled evaluation of particle retention on native corneal tissue under stringent washout conditions, including an additional margin for clearance associated with blinking and drainage. Fluorescence imaging was performed at 1, 1.5, and 2 h after the rinsing began using a Nikon Eclipse Ti fluorescence microscope (Nikon Instruments, Japan) equipped with a FITC filter set. The area of retained fluorescence was determined using ImageJ software by recognizing and processing (Image – Threshold - Area) the fluorescence signal in five random areas of the treated cornea ($6.2*10^4$ μm^2). At each time point, the samples were imaged under identical exposure conditions. A graph of the fluorescence intensity values at different wash time points (0–2 h) was obtained as a function of time. The experiment was performed in five repetitions for each particle type, and data are presented as a mean value ± standard deviation. After cornea treatment and rinsing, the samples were placed on a stub, dehydrated, sputter-coated with gold (Leica EM ACE 600 Sputter Coater, Leica Microsystems, Buffalo Grove, IL, USA), and imaged using a field-emission scanning electron microscope at 3 keV (FEI Quanta 400 ESEM FEG, FEI, Hillsboro, OR, USA).

2.6. In vivo Evaluation

In vivo studies were carried out on normotensive adult male Chinchilla rabbits weighing 2.0–2.5 kg. Animals were kept at 21–23°C and 50–60% humidity. Drinking water and conventional food were provided *ad libitum*. All experiments involving live rabbits were conducted in strict accordance with the Association for Research in Vision and Ophthalmology (ARVO) Statement for the Use of Animals in Ophthalmic and Vision Research (www.arvo.org), and in compliance with the European Convention for the Protection of Vertebrate Animals Used for Experimental and Other Scientific Purposes (ETS 123, Strasbourg). The protocol was approved by the Committee on the Ethics of Animal Experiments of the Helmholtz National Medical Research Center of Eye Diseases (Permit number 22/2 from 05.09.2016).

2.6.1. Intraocular Pressure Measurement

A previously established protocol for topical ocular instillation was used to evaluate and compare the effects of free ENL, M-Vat/ENL, and SM-Vat/ENL on rabbit IOP [22]. At least 3 independent series of experiments for each sample were performed. In each experiment, animals were randomly divided into 3 groups. The first group (5 rabbits, 10 eyes) received single instillations of 50 μL of 2.2 mM ENL in 12.5 mM PBS, pH 7.5, to both eyes. The second and third group (5 rabbits, 10 eyes each) received single instillations of 50 μL of the M-Vat/ENL and SM-Vat/ENL suspensions (pH 7.5), with the same ENL content (which corresponds to approximately ~0.83 mg of particles per eye). The IOP was measured before and after the instillation for 6 h at intervals of 1 h using an automatic veterinary IOP monitor (Tonovet, Tiolat, Finland). This device operates on the rebound measurement principle, in which a lightweight probe makes momentary contact with the corneal surface. The procedure does not require topical anesthesia or animal immobilization, making it well suited for repeated *in vivo* measurements.

2.6.2. Ocular Irritation and Tolerability Assessment

Irritative effects of M-Vat/ENL and SM-Vat/ENL were assessed in healthy Chinchilla rabbits according to the biomicroscopic method for quantitation of ocular toxicity [51]. To estimate the irritative effect, the first group (5 rabbits, 10 eyes) received a single instillation of 50 μL of M-Vat/ENL or SM-Vat/ENL suspension into both eyes. Eye irritation signs (lacrimation, blepharospasm, redness of palpebral conjunctiva, conjunctival and corneal edema, follicular reaction, conjunctival infiltration) were evaluated by slit lamp biomicroscopy (SL−1800, Nidek, Japan) 15 min, 24 h and 48 h after instillation. The second group (5 rabbits, 10 eyes) received the same instillations 3 times per day for 5 days. The eyes were examined under the slit lamp after 24 h and 48 h after the last instillation.

Allergenic effect was estimated *via* the cytologic analyses of conjunctival scrape. Initially, conjunctival scrapes from the lower eyelid were taken with a sterile spatula under topical anesthesia (oxybuprocaine 0.4%) from 15 healthy rabbits. 7 days later, all animals received single instillations of M-Vat/ENL or SM-Vat/ENL suspension to both eyes. Rabbits were divided randomly into 3 groups (5 rabbits, 10 eyes). Conjunctival scrapes from the first group were taken 15 min after the instillation, from the second group – 24 h and from the third group – 48 h after instillation. Scrapes were spread upon the degreased slide, dried on air, fixated in ethanol for 10 min and stained by Romanovsky-Gimza method. Preparations were examined under the light microscope (Mikmed−6, LOMO, Russia), × 400 and × 1000.

2.7. Statistical analysis

All quantitative data are presented as mean ± standard deviation. Data were analyzed using Statistica for Windows (version 10.0, StatSoft Inc., USA). Contact angle data were analyzed using a two-tailed Welch's *t*-test for pairwise comparisons between uncoated and mucin-coated glass substrates within each liquid/suspension group. For each sample and substrate type, 8–12 independent measurements were performed. Bonferroni correction was applied to account for the three pairwise comparisons performed within this dataset, and differences were considered statistically significant at adjusted $p < 0.05$ (exact adjusted p-values are reported in the f2Fig. 2 caption). For *in vivo* IOP measurements, data distribution was not assumed to be normal because of the limited group size (10 eyes); therefore, prespecified pairwise comparisons were performed using the nonparametric two-tailed Mann–Whitney *U* test. The comparisons focused on pharmacologically relevant differences between ENL-loaded formulations and the corresponding comparator groups at matched time points. Differences were considered statistically significant at $p < 0.05$; significance levels are indicated in Fig. 5 as * $p < 0.05$ and ** $p < 0.01$.

3. Results and Discussion

3.1. Engineering of Size-Controlled Porous Vaterite Particles

Two size-controlled porous vaterite fractions were engineered to isolate particle diameter as the primary independent variable governing interfacial behavior on ocular substrates. A micron-sized fraction (M-Vat) and a submicron fraction (SM-Vat) were synthesized under controlled mass crystallization conditions to ensure comparable composition and porosity while varying particle size. SEM analysis (Figs. 1a,b) confirmed spherical morphology with mean diameters of 3.8 ± 0.5 μm (M-Vat) and 0.65 ± 0.15 μm (SM-Vat). Crystallization occurred under highly supersaturated conditions (~10^6), favoring nucleation of metastable vaterite. M-Vat particles exhibited partially

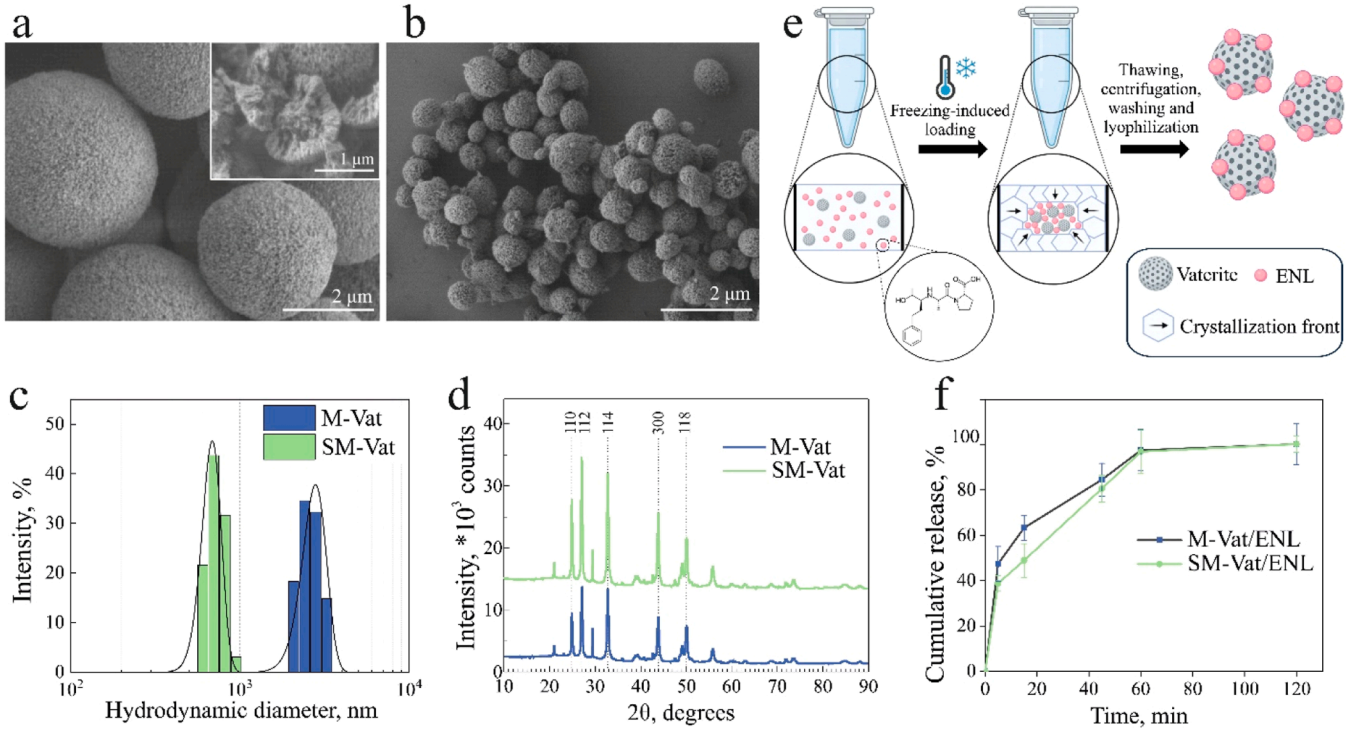

Fig. 1. SEM images of M-Vat (a) and SM-Vat (b), their size distributions (c) and corresponding diffraction patterns (the most prominent vaterite reflections are indexed according to JCPDS No. 00–025–0127) (d); scheme of the freezing-induced loading of ENL into vaterite particles (e), *in vitro* cumulative release profile of ENL from M-Vat/ENL and SM-Vat/ENL (f).

radiating internal patterns characteristic of spherulitic growth, whereas SM-Vat formation likely proceeded via oriented attachment of primary nanocrystals. As supersaturation decreased during growth, the oriented-attachment pathway is gradually superseded by a classical crystal growth, which contributed to radial development of the micron-sized fraction (inset, Fig. 1a). Unimodal size distributions (Fig. 1c) indicated the absence of aggregation in suspension. Hydrodynamic diameters were 5.7 ± 0.6 μm and 0.62 ± 0.08 μm, respectively, in qualitative agreement with SEM while reflecting hydration and dispersion conditions. The ζ-potentials at neutral pH were slightly negative (−8 ± 1 mV for M-Vat and −2 ± 1 mV for SM-Vat), reflecting the presence of an excess of carbonate CO_3^{2-} anions on the particle surface. Rietveld refinement of the obtained XRD patterns (Fig. 1d) confirmed dominant vaterite content (94–96%) with minor calcite fraction in both size groups. Incubation in simulated tear fluid (STF), containing lysozyme, albumin, and mucin, for 6 h did not induce recrystallization (Figure S1), indicating structural stabilization of the vaterite phase by protein adsorption under physiologically relevant conditions. The absence of vaterite-to-calcite transition was further supported by unchanged coherent scattering region sizes: 25 ± 6 nm (intact) vs 24 ± 6 nm (after STF) for M-Vat and 27 ± 8 nm vs 26 ± 7 nm for SM-Vat. The preservation of nanocrystallite dimensions confirms that no internal restructuring occurred during exposure to STF. This structural stability implies maintenance of pore architecture and accessible surface area, which is essential for predictable diffusion-controlled drug loading and release in ocular applications.

Nitrogen adsorption–desorption analysis revealed hierarchical meso–macroporosity in both fractions (Figure S2). For both types of particles, a characteristic hysteresis loop observed at high relative pressures (Figure S2a) indicates the presence of slit-shaped mesopores and interparticle voids. M-Vat exhibited higher specific surface area (35 ± 5 m^2/g) and total pore volume (0.096 cm^3/g) compared to SM-Vat (12 ± 2 m^2/g and 0.023 cm^3/g). This represents a nearly threefold difference in surface area and more than fourfold difference in pore volume. M-Vat displayed a mesopore distribution in the 40–150 Å range, with a clear maximum near 80–100 Å (Figure S2b), favorable for small-molecule loading, whereas SM-Vat demonstrated a broader and flatter pore size distribution extending up to 300 Å. The data indicate that M-Vat particles possess a more developed internal porous structure, whereas SM-Vat particles are likely dominated by surface roughness and interstitial voids between loosely packed nanograins. Thus, the surface area of SM-Vat is primarily external, whereas in M-Vat it mainly originates from an internal mesoporous network. Notably, despite the pronounced differences in total surface area and pore volume, both fractions preserve a mesopore population within the ~50–150 Å range (Figure S2b), which is most relevant for adsorption and diffusion of small hydrophilic molecules such as ENL. Therefore, the internal architecture differs in magnitude (total pore volume), but the presence of an accessible mesoporous domain is conserved between M-Vat and SM-Vat.

Enalaprilat (ENL), a small hydrophilic molecule, was incorporated into both particle types by freezing-induced loading that was intentionally optimized to achieve comparable drug loading levels despite the differences in pore volume between M-Vat and SM-Vat (Fig. 1e). Final encapsulation efficiencies were of 33 ± 9% for M-Vat and 21 ± 16% for SM-Vat, while loading capacities were comparable: 5.2 ± 1.5 wt% and 4.7 ± 2.1 wt%, respectively. The different initial particle-to-drug mass ratios were therefore used to compensate for differences in porous architecture and accessible pore volume, enabling comparison at comparable final ENL payloads rather than identical loading inputs. This convergence in loading suggests that freezing-induced loading is governed mainly by ENL partitioning into accessible mesoporous/void spaces rather than by total pore volume alone. Zeta potential remained unchanged after loading (−7 ± 1 and −2 ± 1 mV for M-Vat and SM-Vat, respectively), indicating minimal surface chemistry alteration. Table 1 provides a comprehensive overview of the particle characterization described above.

Release studies (Figure 1f) revealed a slightly faster initial release from M-Vat, consistent with its higher internal mesoporosity and greater fraction of accessible internal pores. Release profiles were fitted using conventional kinetic models for porous matrices (Table 2). Model

Table 1
Characteristics of the particles.

Parameter	M-Vat	SM-Vat
Diameter according to SEM, μm	3.8 ± 0.5	0.65 ± 0.15
Hydrodynamic diameter, μm	5.7 ± 0.6	0.62 ± 0.08
PDI	0.33	0.37
ζ-potential, mV	−8 ± 1	−2 ± 1
Vaterite/calcite ratio	94.9% / 5.1%	95.9% / 4.1%
Coherent scattering region size, nm	25 ± 6	27 ± 8
Specific surface area, m^2/g	35 ± 5	12 ± 2
Pore volume, cm^3/g	0.096	0.023
ENL encapsulation efficiency, %	33 ± 9	21 ± 16
ENL loading capacity, wt%	5.2 ± 1.5	4.7 ± 2.1
ζ-potential of the ENL-loaded particles, mV	−7 ± 1	−2 ± 1

comparison indicated diffusion-dominated release behavior, in agreement with previous reports [52,53]. The Higuchi model provided the best fit for ENL release from both M-Vat and SM-Vat. The comparable Higuchi constants suggest similar effective diffusion rates despite differences in total pore volume. Moreover, the Korsmeyer–Peppas exponent values ($n < 0.5$) indicate Fickian-type transport, supporting the view that ENL release is primarily governed by diffusion from accessible mesopores and interparticle voids along the concentration gradient, rather than being controlled by particle recrystallization, dissolution, or total porosity alone.

Collectively, both fractions exhibit comparable phase composition, surface chemistry, drug loading capacity, and diffusion-controlled release, while differing primarily in particle diameter and internal pore architecture. The preserved diffusion-driven release and similar effective diffusion constants minimize formulation-dependent bias, thereby isolating particle size as the principal variable for subsequent evaluation of interfacial retention under shear flow.

3.2. *Mucoadhesive Interfacial Retention Under Tear-Mimicking Flow*

Particle retention under ocular clearance-relevant shear flow was assessed using mucin-coated glass substrates as a simplified model of the ocular mucosal surface. Mucin represents the principal structural component of the tear film glycocalyx and exhibits strong affinity toward calcium-containing materials, including vaterite [28]. Therefore, this model provides a controlled platform for assessing the interfacial retention potential of M-Vat and SM-Vat particles under physiologically relevant conditions. The presence of a continuous mucin layer on the glass surface was qualitatively confirmed by spectrophotometry (Figure S3a) and quantitatively verified by gravimetric measurement (Figure S3b), ensuring consistent and reproducible surface coverage.

3.2.1. *Surface Properties and Interfacial Interactions*

To investigate the mechanisms underlying particle retention on mucosal-mimicking surfaces, the wetting behavior of the suspensions was evaluated by measuring the static contact angle θ of droplets deposited on mucin-coated glass substrates (Fig. 2a,b). Representative side-view images (Fig. 2a) illustrate pronounced droplet flattening on mucin-coated substrates compared to the more hemispherical profiles observed on uncoated glass. In the context of mucoadhesion, lower contact angles reflect improved spreading and stronger interfacial interaction with the mucosal surface. On mucin-coated surfaces, droplets exhibited a gradual decrease in contact angle over ~3 min before reaching equilibrium (Figure S4), whereas on uncoated glass stabilization occurred immediately. This time-dependent spreading indicates active interaction between the liquid phase and the mucin layer. Water diffusion into the mucin film induces polymer swelling and partial liquid absorption, leading to progressive hydration and interpenetration at the interface. During this process, vaterite particles penetrate the hydrated glycoprotein network and become temporarily immobilized via Ca^{2+}–mucin coordination (carboxylate and sialic acid residues [28]), complemented by electrostatic attraction, hydrogen bonding, and steric entanglement with mucin fibrils. The observed dynamic flattening therefore reflects mucoadhesive interfacial interactions rather than simple physical wetting, as further corroborated by dynamic washout analysis presented below.

As shown in Fig. 2b, mucin coating substantially reduced the contact angle for all tested suspensions, confirming the formation of a

Table 2
Approximation of the ENL release data using different mathematical models. K is a rate constant, n is a release exponent and R^2 is a correlation coefficient.

Mathematical models and its parameters	Korsmeyer-Peppas $\frac{M_t}{M_\infty} = K_{KP} \cdot t^n$			Higuchi $\frac{M_t}{M_\infty} = K_H \cdot t^{\frac{1}{2}}$		First-order $\ln\left(1 - \frac{M_t}{M_\infty}\right) = K_1 \cdot t$		Hixson -Crowell $\left(1 - \frac{M_t}{M_\infty}\right)^{\frac{1}{3}} = 1 - K_\beta \cdot t$	
	K	n	R^2	K	R^2	K	R^2	K	R^2
SM-Vat	$2.2 \bullet 10^{-3}$	0.33	0.95	$1.1 \bullet 10^{-3}$	0.99	$1.7 \bullet 10^{-2}$	0.99	$3.5 \bullet 10^{-5}$	0.98
M-Vat	$3.1 \bullet 10^{-3}$	0.26	0.98	$9 \bullet 10^{-4}$	0.99	$1.21 \bullet 10^{-2}$	0.95	$2.9 \bullet 10^{-5}$	0.98

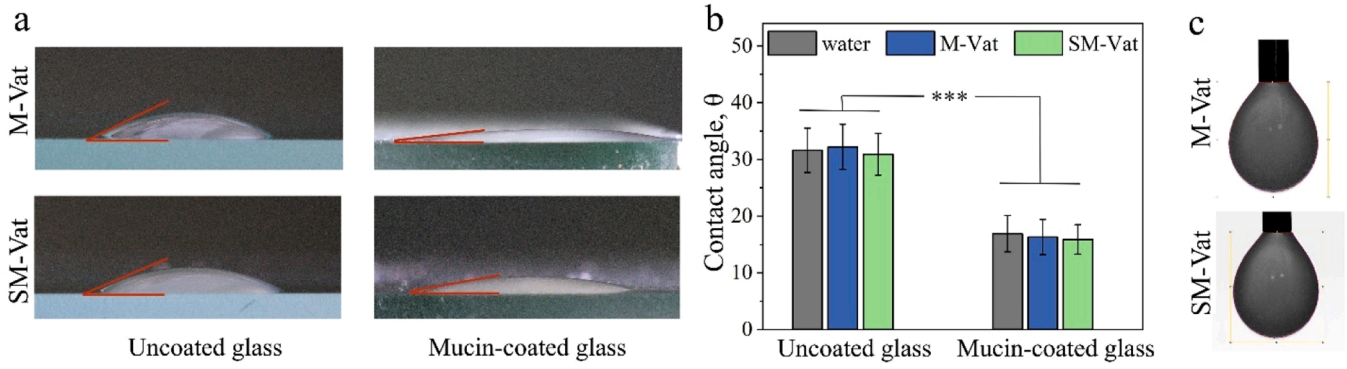

Fig. 2. Representative side-view images acquired 3 min after droplet deposition, indicating reduced contact angle on mucin-coated glass (a). Static contact angles of PBS, M-Vat, and SM-Vat suspensions on uncoated and mucin-coated substrates. Data are presented as mean ± SD, n = 8–12 independent droplet images per group. Statistical comparisons were performed between uncoated and mucin-coated substrates within each group using a two-tailed Welch's *t*-test with Bonferroni correction. *** adjusted $p < 0.001$ (exact adjusted p-values: PBS, $p = 1.55 \times 10^{-8}$; M-Vat, $p = 3.65 \times 10^{-8}$; SM-Vat, $p = 8.80 \times 10^{-7}$) (b). Representative pendant-drop images of M-Vat, and SM-Vat suspensions used for the surface tension measurements (c).

hydrophilic glycoprotein layer that promotes aqueous spreading. The mean contact angle decreased by ~15° compared to uncoated glass, consistent with previously reported data for mucin-coated surfaces [54]. For both M-Vat and SM-Vat suspensions in PBS, θ on mucin-coated glass (≈15°) was approximately half of that measured on uncoated glass (≈31°), indicating markedly enhanced wettability. Importantly, the contact angles of both suspensions were indistinguishable from that of PBS (Figure S5) on both substrates, demonstrating that the presence of particles at 16 mg/mL does not alter the intrinsic wetting behavior of the liquid phase.

Surface tension measurements using the pendant drop method (Fig. 2c) showed values of 61.1 ± 0.8 mN/m for M-Vat and 61.4 ± 1.0 mN/m for SM-Vat suspensions, compared to 70.7 ± 1.3 mN/m for PBS. The moderate reduction relative to PBS indicates limited particle–air interface activity and confirms preserved colloidal stability and fluidity. Although higher than the physiological surface tension of tears (≈40–46 mN/m), these values fall within the clinically validated range of ophthalmic formulations (34–71 mN/m) [55–57].

Using the measured surface tension and equilibrium contact angle on mucin-coated glass, the work of adhesion, W_a, was estimated to be approximately 120 mN/m for both M-Vat and SM-Vat suspensions. These comparable values indicate similar macroscopic interfacial energetics, suggesting that the observed differences in dynamic retention arise primarily from particle size rather than differences in wetting or adhesion.

3.2.2. Size-Dependent Mucoadhesion Under Dynamic Flow Conditions

To quantify dynamic interfacial stability, particle retention was evaluated on mucin-coated and uncoated glass substrates under continuous rinsing with simulated tear fluid (STF, 10 mL/min), corresponding to shear conditions substantially exceeding physiological tear turnover (~5000–10000 × above natural tear flow) (Fig. 3a). Fluorescence microscopy (Figure S6) was used to monitor the retention of FITC–dextran-labeled M-Vat and SM-Vat particles over time. The decay of fluorescence intensity was fitted using a single-exponential model to determine washout rate constants *k*, that characterize particle detachment under flow. Retention strongly depended on both particle size and the presence of mucin (Fig. 3b). On mucin-coated substrate, after 1 h of rinsing, ~30–40% of SM-Vat particles remained adhered, whereas M-Vat retention decreased below 20%. The washout rate constant of SM-Vat was approximately half that of M-Vat ($k_{SM} \approx 0.65\ h^{-1}$ vs $k_M \approx 1.16\ h^{-1}$), corresponding to characteristic half-lives of ~1.1h and ~0.6h, respectively. Thus, the submicron fraction persisted ~1.8-fold longer under shear flow.

Because surface chemistry and interfacial energetics (contact angle, surface tension, work of adhesion) were comparable between fractions, the observed difference in washout kinetics indicates a size-dependent mechanical origin of detachment. Particle removal occurred predominantly *via* abrupt lift-off rather than gradual sliding, consistent with hydrodynamic torque overcoming adhesive stabilization, as previously reported for mucin-coated systems [54]. This behavior can be rationalized by considering the balance between hydrodynamic and adhesive contributions (Fig. 3c). Under shear flow, the drag force scales approximately as $F_d \sim D^2$, where D is the particle diameter, while the resulting hydrodynamic torque scales as $M_{hyd} \sim D^3$. Adhesive stabilization depends on the effective contact region A_c between the particle and the compliant mucin layer. Because the mucin network undergoes finite deformation and does not form a fully rigid contact interface, the real contact region scales sub-quadratically with particle diameter and can be approximated as $A_c \sim D$. The adhesive force therefore scales as $F_{adh} \sim W_a A_c \sim W_a D$, where W_a is the work of adhesion determined in Section 3.2.1. Accordingly, the corresponding adhesive moment scales as $M_{adh} \sim W_a D^2$. Consequently, the ratio of destabilizing to stabilizing torque increases approximately linearly with particle diameter: $M_{hyd}/M_{adh} \sim D$.

Using this scaling framework, the detachment propensity for M-Vat is predicted to be ~5.9 times higher than for SM-Vat based on SEM diameters and ~9.2 times higher based on hydrodynamic diameters. This theoretical trend is consistent with the experimentally observed faster washout of the larger fraction, although the magnitude is moderated by size polydispersity and interfacial heterogeneity. Control experiments on uncoated glass revealed rapid clearance for both fractions, with more than 60% of particles removed within the first 10 min, confirming that dynamic stabilization originates from specific mucin-particle interactions rather than nonspecific substrate adhesion. Collectively, these results demonstrate that mucin-mediated anchoring enables resistance to mechanical clearance and that particle size functions as a governing design parameter controlling interfacial persistence under shear flow.

3.2.3. Ex Vivo Corneal Retention under Accelerated Tear Flow

To determine whether the size-dependent mechanical stabilization observed on model mucin substrates translates to a physiologically relevant interface, particle retention was evaluated on freshly excised rabbit corneas under continuous rinsing with STF. A fluorescence-based flow-through assay was employed to quantify corneal retention under accelerated clearance conditions (~50–100-fold higher than physiological tear turnover). Immediately after topical administration, both FITC-dextran labeled M-Vat and SM-Vat formed well-defined deposition areas on the corneal surface (Fig. 4a), which were used as regions of interest for quantitative analysis.

Representative confocal images acquired during rinsing (Fig. 4b) demonstrate progressive fluorescence loss over time, indicating gradual particle removal. After 2 h of continuous flow, both formulations exhibited substantial signal reduction. Quantitative analysis (Fig. 4c),

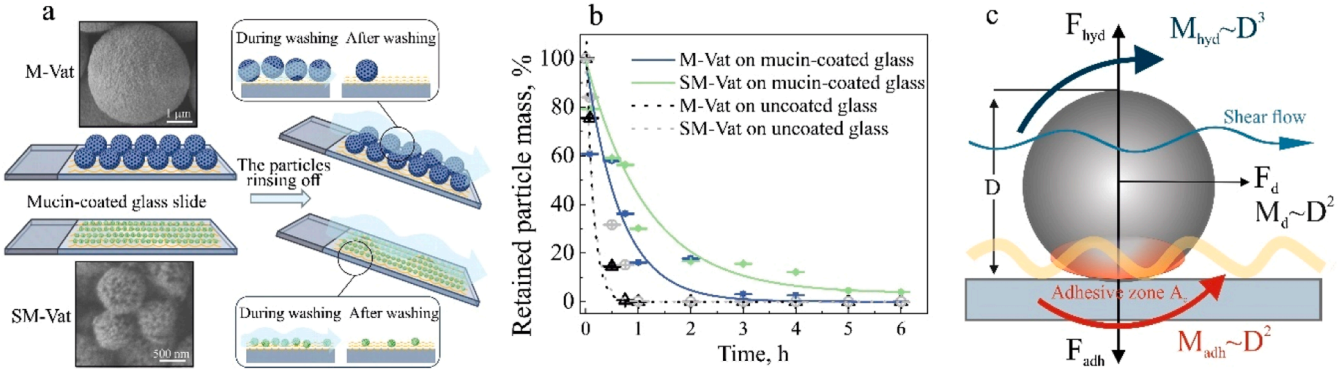

Fig. 3. Interfacial retention of porous vaterite particles under simulated tear flow. SEM-images of M-Vat and SM-Vat and schematic representation of the experimental washout setup on mucin-coated glass substrates during and after rinsing (a); washout kinetics of M-Vat and SM-Vat from mucin-coated and uncoated glass under continuous flow, expressed as retained particle mass versus time. (mean ± SD, n = 5) (b); mechanistic illustration of size-dependent detachment under shear flow, highlighting the balance between hydrodynamic and adhesive torques governing particle lift-off at the mucin interface (c).

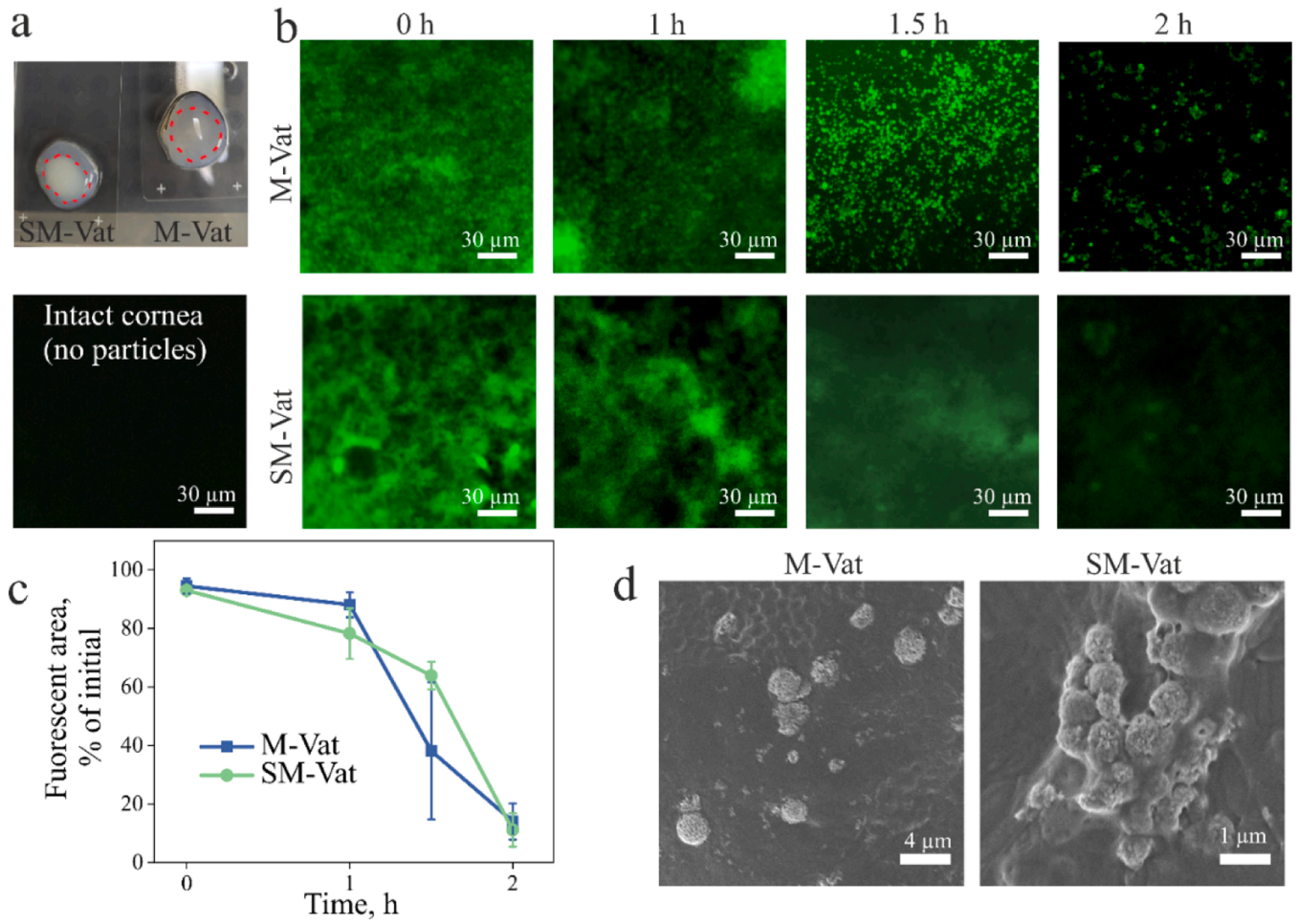

Fig. 4. *Ex vivo* evaluation of corneal retention of FITC-dextran labeled M-Vat and SM-Vat particles. Brightfield image of excised rabbit corneas immediately after topical administration of SM-Vat and M-Vat, red dashed lines outline the initial droplet deposition area (a); confocal fluorescence images of corneal surfaces over a 2-hour rinsing period with STF under accelerated flow (50–100-fold above physiological tear turnover), recorded at 0, 1, 1.5, and 2 h. An intact cornea without particles is shown as a negative control (b); quantitative analysis of retained fluorescent area expressed as a percentage of the initial coverage (mean ± SD, n = 5) (c); SEM images of the corneal surface after 2 h of rinsing showing retained particles (d).

where the mean percentage of the corneal surface covered by fluorescent particles is plotted against rinsing time for both formulations, revealed no statistically significant difference between M-Vat and SM-Vat retention throughout the experiment. Approximately 10% of the initially covered corneal area remained occupied by particles after 2 h of accelerated rinsing. The absence of a statistically significant size-dependent difference contrasts with the controlled shear experiments on mucin-coated glass (Section 3.2.2), where SM-Vat exhibited slower washout than M-Vat. This apparent discrepancy can be explained by differences in both interfacial complexity and measurement readout. The mucin-coated glass model represents a simplified, rigid, and relatively homogeneous substrate, where particle detachment is mainly governed by hydrodynamic torque and mucin-mediated adhesion; retention was quantified from total fluorescence loss and washout kinetics. In contrast, the *ex vivo* cornea is a heterogeneous biological interface containing epithelial microtopography, membrane-associated mucins, residual tear-film proteins, lipids, and glycoproteins, which can promote local trapping and embedding of both particle fractions. Moreover, *ex vivo* retention was quantified as residual fluorescent coverage area rather than total retained particle mass, potentially reducing sensitivity to size-dependent differences in particle number or mass. Therefore, the convergence of M-Vat and SM-Vat retention *ex vivo* likely reflects biological interfacial heterogeneity masking the purely mechanical size effect observed *in vitro*.

SEM analysis (Fig. 4d) confirmed the presence of residual particles on the corneal surface after 2 h of rinsing. Importantly, the particles retained their characteristic spherical vaterite morphology and showed no signs of recrystallization. Preservation of morphology and polymorphic composition in both size groups indicates structural stability of porous vaterite in tear film conditions. This stability can be attributed to interfacial adsorption of tear proteins and other film components, which likely form a protective corona that kinetically suppresses phase transformation and dissolution. Notably, M-Vat predominantly present as discrete surface-attached particles, whereas SM-Vat partially embedded within a surface-associated biofilm, further supporting the role of biological matrix interactions in modulating detachment behavior.

3.3. *In Vivo Pharmacodynamic Validation of the Retention Strategy*

The interfacial studies presented above demonstrate that submicron particles exhibit mechanically enhanced stabilization under shear and maintain structural integrity on the native ocular surface. However, prolonged interfacial persistence is therapeutically relevant only if it is associated with improved pharmacodynamic performance. We therefore evaluated whether retention-driven strategy enhances the intraocular pressure (IOP)-lowering efficacy of enalaprilat (ENL) *in vivo*.

Preliminary screening of ACE inhibitors demonstrated that ENL produced the most pronounced and sustained IOP reduction in rabbits [30]. Therefore, ENL was incorporated into the M-Vat and SM-Vat particles, and the formulations (free ENL, M-Vat/ENL, and

SM-Vat/ENL) were administered topically to normotensive rabbit eyes. IOP was measured at predefined time points using tonometry to assess both the magnitude and duration of the pressure-lowering effect (Fig. 5a). The temporal profiles of IOP reduction are presented in Fig. 5b. SM-Vat/ENL produced the most pronounced and sustained hypotensive effect among the tested formulations. Statistically significant IOP reductions were detected at 1–5 h post-instillation according to prespecified Mann–Whitney U comparisons, with significance levels indicated in Fig. 5b. Although all groups reached maximal effect at approximately 3 h, the submicron formulation produced a greater magnitude and longer duration of pressure reduction. By 6 h, the effects of all formulations converged, consistent with drug elimination and the expected pharmacological window [32].

Box-and-whisker analysis at the 3 h time point (Fig. 5c) further highlights differences in therapeutic consistency. Free ENL exhibited substantial variability (median −2.5 mmHg, mean −2.3 ± 0.4 mmHg), with several low-response outliers. M-Vat/ENL showed comparable variability (median −1.8 mmHg, mean −2.0 ± 0.4 mmHg). In contrast, SM-Vat/ENL demonstrated a greater median reduction (−3.0 mmHg, mean −3.4 ± 0.3 mmHg), reduced variability and absence of near-zero responders, suggesting improved consistency of the pharmacodynamic response.

To quantify overall therapeutic impact, the area under the IOP reduction curve (AUC) was calculated (Fig. 5d). This metric captures both the magnitude and duration of the therapeutic response. When normalized to the free ENL group (set to 100%), SM-Vat/ENL achieved ~210%, corresponding to an approximately 2.1-fold higher cumulative pharmacodynamic effect. In contrast, M-Vat/ENL produced an AUC comparable to that of the free drug. These findings support an association between the enhanced interfacial persistence of the submicron fraction and improved pharmacodynamic efficacy *in vivo*. Although direct ocular pharmacokinetic measurements were not performed, equivalent ENL dosing and comparable release profiles suggest that the enhanced IOP-lowering effect is likely retention-associated rather than dose-driven.

3.4. Biocompatibility and Ocular Safety

While enhanced interfacial stabilization was associated with improved *in vivo* pharmacodynamic performance, successful clinical translation requires rigorous safety validation across multiple biological levels. Ocular formulations must demonstrate compatibility not only with isolated cell systems but also with the intact ocular surface under repeated exposure conditions. Therefore, we performed a comprehensive safety assessment encompassing cellular uptake and cytocompatibility, hemocompatibility under conservative systemic-exposure scenarios, and *in vivo* ocular tolerability following repeated topical administration.

3.4.1. Cellular Uptake and Cytocompatibility

Two ocular cell models were selected: human lens epithelial cells (HLEpiC), representing a sensitive intraocular cell type critical for

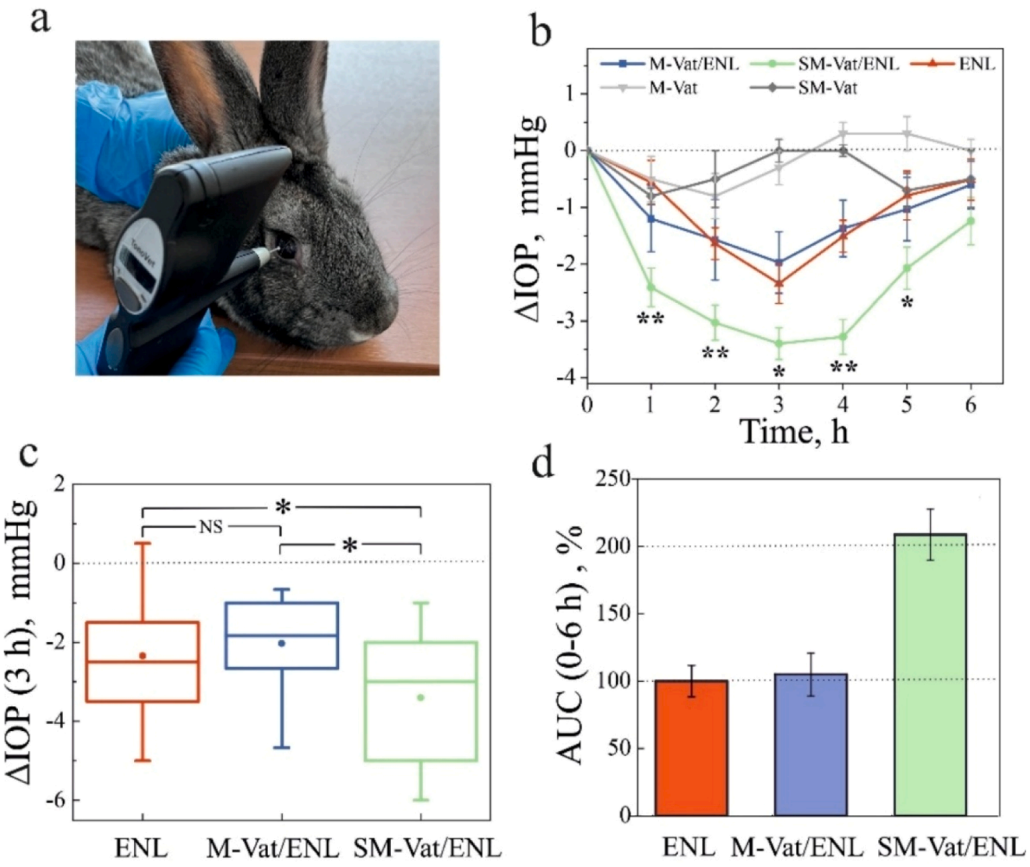

Fig. 5. *In vivo* IOP-lowering efficacy of ENL-loaded vaterite formulations. Rebound tonometry measurement of IOP in normotensive rabbits following topical administration (a); time-course of IOP reduction over 6 h after single instillation of free ENL, M-Vat/ENL and SM-Vat/ENL formulations. M-Vat and SM-Vat without drug served as particle-only controls. Data are presented as mean ± SD, n = 10 eyes per group. Statistical comparisons were performed using a two-tailed Mann–Whitney *U* test; * $p < 0.05$, ** $p < 0.01$ (b); box-and-whiskers plot for IOP reduction after 3 h post-instillation. Boxes represent the 25th – 75th percentile range, the line bisecting the box represents the median, the dot denotes the mean, and whiskers indicate the 5th and 95th percentiles. Prespecified pairwise comparisons were performed using a two-tailed Mann–Whitney *U* test; * $p < 0.05$, NS, not significant (c); relative area under the IOP-reduction curve over 6 h normalized to free ENL group (100%) (d).

maintaining lens transparency and homeostasis, and human corneal epithelial cells (HCE-T), corresponding to the primary barrier exposed to topical formulations. Based on drug loading efficiency, *in vivo* therapeutic dosing, and estimated ocular exposure, an equivalent particle concentration of approximately 40 μg/well was calculated for *in vitro* testing. To assess concentration-dependent effects, cells were incubated with 10, 50, and 100 μg/well of particles. Fluorescence microscopy revealed efficient cellular association of FITC-labeled M-Vat and SM-Vat without detectable morphological alterations (Fig. 6a). Orthogonal confocal views confirmed intracellular localization in both HLEpiC and HCE-T cells (Fig. 6b).

Quantitative CCK−8 analysis demonstrated preserved viability in both HLEpiC and HCE-T cell cultures after 24 h of incubation with M-Vat and SM-Vat (Figure S7 for 2D and 3D cell culture) and M-Vat/ENL and SM-Vat/ENL (Fig. 6c for 2D cell culture). Cell viability remained $\geq$ 70% across all concentrations, with no statistically significant size-dependent cytotoxicity observed. In 3D HLEpiC spheroids, both particle fractions penetrated the outer cellular layers in a dose-dependent manner (Fig. 6d–f). At 10 μg/well, fluorescence levels were comparable to control, whereas 50 and 100 μg/well resulted in markedly increased signal intensity. To confirm that the fluorescence was specifically caused by particle penetration, the spheroids were fixed, and their surface examined by SEM (Fig. 6g). SEM analysis confirmed particle adhesion and partial embedding within the spheroid surface architecture, indicating compatibility with multicellular tissue-like constructs.

Although systemic exposure following topical administration is expected to be minimal, erythrocyte compatibility was evaluated to address a conservative worst-case scenario involving nasolacrimal drainage. The assay was performed at particle concentrations up to 0.1 mg/mL, exceeding the levels that could realistically reach systemic circulation. Both M-Vat and SM-Vat exhibited hemolysis rates below 2% across the tested range (Figure S8), classifying them as non-hemolytic according to ASTM-F765 criteria. These results align with previous reports on calcium carbonate-based carriers, which demonstrated hemolysis levels below 2–5% even at substantially higher concentrations up to 1–2 mg/mL [46,58,59]. Collectively, the in vitro and hemocompatibility data confirm efficient cellular interaction without cytotoxic or hemolytic effects, supporting the translational safety profile of the developed formulations.

3.4.2. *In Vivo Ocular Tolerability*

Although *in vitro* assays demonstrated favorable cellular compatibility, translation to the ocular surface requires confirmation of tissue-level tolerability under dynamic tear flow and repeated dosing conditions. Ocular tolerability was therefore evaluated *in vivo* following single and repeated instillations, focusing on clinical signs of irritation, epithelial integrity, and inflammatory response. No clinical signs of irritation were observed. Representative images acquired 24 h after instillation of SM-Vat/ENL show normal external ocular appearance without conjunctival hyperemia or discharge (Fig. 7a). The eyes were examined under the slit lamp after 24 h and 48 h after the last instillation. The corneal surface appeared optically clear, with no signs of edema or epithelial disruption, no fluorescein staining (Fig. 7b), indicating preserved epithelial integrity. To assess potential inflammatory or allergic responses, conjunctival scrapings were collected at 15 min, 24 h, and 48 h following administration. Cytological examination revealed intact epithelial cells and occasional small lymphocytes, with no eosinophils, basophils, mast cells, or other inflammatory infiltrates (Fig. 7c). The cytological profile remained indistinguishable from untreated controls, confirming the absence of mucosal irritation or immune activation. From a mechanical perspective, both particle fractions remain below the commonly reported 5–10 μm threshold associated with foreign-body sensation and corneal microtrauma [60,61], supporting mechanical tolerability. Importantly, the ocular safety of $CaCO_3$ particles is further supported by a prior controlled clinical study in which $CaCO_3$ particles were applied topically at concentrations exceeding 100 mg/mL (over six times higher than in our suspensions) without adverse effects [62], providing an additional safety margin relative to the present formulations. Collectively, the clinical, cytological, and morphological assessments demonstrate excellent ocular tolerability of both M-Vat/ENL and SM-Vat/ENL formulations.

4. Conclusion

In this work, we demonstrate that interfacial retention of particulate drug carriers at the ocular surface is governed by a size-dependent balance between hydrodynamic detachment and adhesive stabilization under tear flow. By engineering structurally equivalent vaterite particles that differ primarily in diameter while preserving physicochemical properties, drug loading, and diffusion-controlled release, we identify particle size as a key parameter controlling interfacial behavior.

Under controlled shear conditions, submicron particles exhibited markedly enhanced retention due to reduced hydrodynamic torque, supporting the conclusion that detachment probability increases with particle size. However, *ex vivo* experiments on native corneal tissue revealed a transition from physics-dominated to biology-dominated retention, where protein adsorption, interfacial restructuring, and tear film complexity attenuate purely geometric scaling effects. This shift highlights the limitation of simplified *in vitro* models and underscores the necessity of integrating multiscale interfacial analysis. Crucially, this interfacial behavior was associated with improved therapeutic outcome. Submicron enalaprilat-loaded vaterite particles produced an approximately twofold higher cumulative pharmacodynamic effect and a more consistent IOP-lowering profile *in vivo*, whereas micron-sized counterparts showed no clear benefit over the free drug. These findings suggest a pharmacodynamic association between interfacial retention and *in vivo* efficacy.

Taken together, our results move beyond empirical optimization of mucoadhesive formulations and introduce a mechanistic framework for the rational design of ocular drug delivery systems based on control of hydrodynamic detachment under flow. Particle size is identified as a critical and previously underappreciated design parameter for inorganic carriers. The proposed relationship between particle size, interfacial retention, and pharmacodynamic performance provides a generalizable design principle for mucosal drug delivery systems, where rapid clearance remains a fundamental barrier to therapeutic efficiency.

CRediT authorship contribution statement

Tatiana Pallaeva: Writing – original draft, Visualization, Validation, Resources, Investigation. **Vladimir Artemov:** Writing – original draft, Validation, Methodology, Investigation. **Daria Trushina:** Writing – review & editing, Writing – original draft, Supervision, Resources, Project administration, Methodology, Investigation, Funding acquisition, Formal analysis, Data curation, Conceptualization. **Aleksander Mikheev:** Writing – original draft, Visualization, Validation, Methodology, Investigation, Formal analysis, Data curation. **Tatiana Bukreeva:** Writing – original draft, Supervision, Resources. **Xiangzhong Chen:** Writing – review & editing, Supervision, Resources. **Caihong Zhu:** Writing – review & editing, Supervision. **Ivan Burmistrov:** Writing – original draft, Visualization, Validation, Methodology. **Ivan Kasyanov:** Writing – review & editing, Writing – original draft, Visualization, Validation, Methodology, Investigation. **Olga Beznos:** Writing – original draft, Visualization, Methodology, Investigation, Formal analysis, Data curation. **Abalymov Abalymov:** Writing – review & editing, Writing – original draft, Visualization, Validation, Supervision, Methodology, Investigation. **Ekaterina Popova:** Writing – original draft, Visualization, Validation, Formal analysis. **Olga Kost:** Writing – original draft, Visualization, Methodology, Investigation.

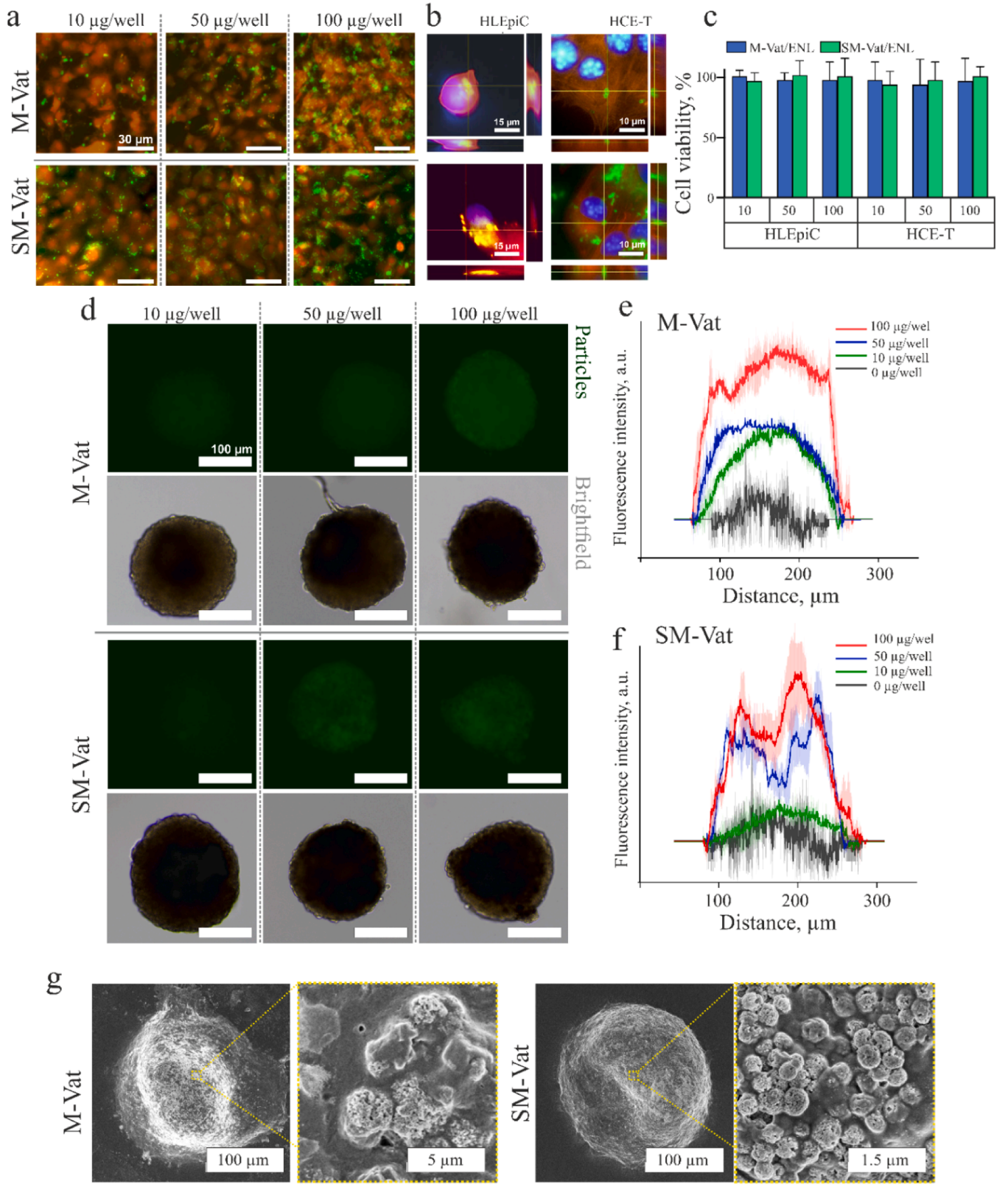

Fig. 6. Representative fluorescent images of HLEpiC cells incubated with 10, 50, and 100 µg/well FITC-dextran labeled particles. Cells are stained with Calcein Red-Orange (red); particles appear green. Scale bar: 30 µm (a); orthogonal confocal views of HLEpiC and HCE-T cells with internalized particles. Scale bars:15 µm (b); cell viability of HLEpiC and HCE-T after 24 h exposure to M-Vat/ENL and SM-Vat/ENL at indicated concentrations (mean ± SD) (c); fluorescence and corresponding brightfield images of HLEpiC spheroids after incubation with 10, 50, and 100 µg/well of particles (in green). Scale bar: 100 µm (d); radial fluorescence intensity profiles of HLEpiC spheroids after incubation with 10, 50, and 100 µg/well of particles (e-f); SEM images of HLEpiC spheroids after incubation with 50 µg/well particles, confirming surface association and partial embedding (g).

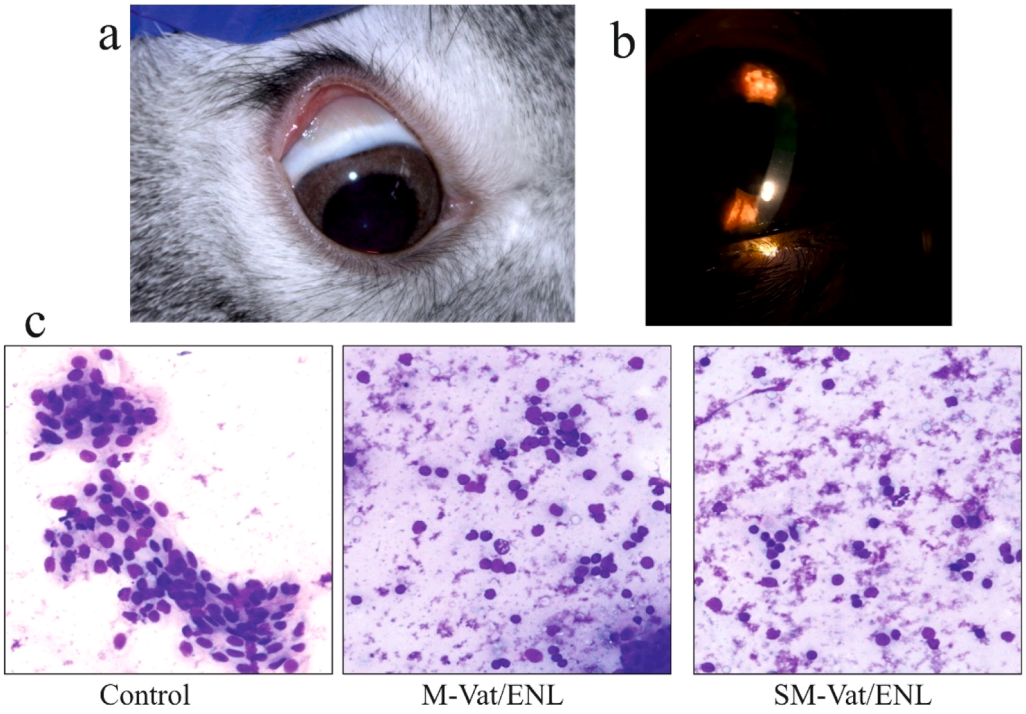

Fig. 7. *In vivo* ocular tolerability of ENL-loaded vaterite formulations. Representative image of rabbit eye 24 h after SM-Vat/ENL administration, showing absence of conjunctival irritation (a); slit-lamp biomicroscopy of the cornea 24 h post-treatment demonstrating preserved epithelial integrity and absence of fluorescein staining (b); conjunctival scrapes from untreated control and 48 h after M-Vat/ENL and SM-Vat/ENL treatment, showing no inflammatory cell infiltration (c).

Declaration of Competing Interest

The authors declare that they have no known competing financial interests or personal relationships that could have appeared to influence the work reported in this paper.

Acknowledgements

The work was carried out within the state assignment of NRC "Kurchatov Institute" using the equipment of Shared Research Center "Structural diagnostics of materials" of the Kurchatov Complex Crystallography and Photonics NRC “Kurchatov institute” under support of Ministry of science and higher education of the Russian Federation within the state assignment of NRC "Kurchatov Institute”. The authors would like to acknowledge the Faculty of Chemistry Lomonosov Moscow State University (State assignment project №121041500039–8) for providing materials for analytical measurements. Abalymov A. acknowledges the National Postdoctoral Program for Innovative Talents and the Foreign Expert Program (No. Y20240176) of Ministry of Human Resources and Social Security (China) for supporting cell-based experimental work. Trushina D. acknowledges Shanghai Municipal Science and Technology Program (“Shanghai Sci-tech Co-Research Program”, 25HB2716400) for supporting the 3D cell spheroid experiments.

Appendix A. Supporting information

Supplementary data associated with this article can be found in the online version at doi:10.1016/j.colsurfb.2026.115967.

Data availability

No data was used for the research described in the article.

References

[1] J.D. Steinmetz, R.R.A. Bourne, P.S. Briant, et al., Causes of blin dness and vision impairment in 2020 and trends over 30 years, and prevalence of avoidable blindness in relation to VISION 2020: the Right to Sight: an analysis for the Global Burden of Disease Study, Lancet Glob. Health 9 (2021) e144–e160, https://doi.org/10.1016/S2214-109X(20)30489-7.

[2] J.B. Jonas, T. Aung, R.R. Bourne, A.M. Bron, R. Ritch, S. Panda-Jonas, Glaucoma, Lancet 390 (2017) 2183–2193, https://doi.org/10.1016/S0140-6736(17)31469-1.

[3] K. Glover, D. Mishra, S. Gade, L.K. Vora, Y. Wu, A.J. Paredes, R.F. Donnelly, T.R. R. Singh, Microneedles for advanced ocular drug delivery, Adv. Drug. Deliv. Rev. 201 (2023) 115082, https://doi.org/10.1016/j.addr.2023.115082.

[4] Y. Yang, A. Lockwood, Topical ocular drug delivery systems: Innovations for an unmet need, Exp. Eye Res. 218 (2022) 109006, https://doi.org/10.1016/j.exer.2022.109006.

[5] E.M. Del Amo, Topical ophthalmic administration: Can a drug instilled onto the ocular surface exert an effect at the back of the eye? Front. Drug. Deliv. 2 (2022) 954771 https://doi.org/10.3389/fddev.2022.954771.

[6] X. Zhou, D. Zhou, X. Zhang, Y. Zhao, L. Liao, P. Wu, B. Chen, X. Duan, Research progress of nano delivery systems for intraocular pressure lowering drugs, Heliyon 10 (2024) e32602, https://doi.org/10.1016/j.heliyon.2024.e32602.

[7] B. Silva, B. São Braz, E. Delgado, L. Gonçalves, Colloidal nanosystems with mucoadhesive properties designed for ocular topical delivery, Int. J. Pharm. 606 (2021) 120873, https://doi.org/10.1016/j.ijpharm.2021.120873.

[8] Q. Qi, Y. Wei, X. Zhang, J. Guan, S. Mao, Challenges and strategies for ocular posterior diseases therapy via non-invasive advanced drug delivery, J. Control. Release 361 (2023) 191–211, https://doi.org/10.1016/j.jconrel.2023.07.055.

[9] E.V. Popova, V.E. Tikhomirova, O.V. Beznos, N.B. Chesnokova, Y.V. Grigoriev, N. L. Klyachko, O.A. Kost, Chitosan-covered calcium phosphate particles as a drug vehicle for delivery to the eye, Nanomed. Nanotechnol. Biol. Med. 40 (2022) 102493, https://doi.org/10.1016/j.nano.2021.102493.

[10] S.-N. Kim, S.A. Ko, C.G. Park, S.H. Lee, B.K. Huh, Y.H. Park, Y.K. Kim, A. Ha, K. H. Park, Y.B. Choy, Amino-Functionalized Mesoporous Silica Particles for Ocular Delivery of Brimonidine, Mol. Pharm. 15 (2018) 3143–3152, https://doi.org/10.1021/acs.molpharmaceut.8b00215.

[11] L.-J. Luo, D.D. Nguyen, J.-Y. Lai, Dually functional hollow ceria nanoparticle platform for intraocular drug delivery: A push beyond the limits of static and dynamic ocular barriers toward glaucoma therapy, Biomaterials 243 (2020) 119961, https://doi.org/10.1016/j.biomaterials.2020.119961.

[12] R. Chen, Y. Qian, R. Li, Q. Zhang, D. Liu, M. Wang, Q. Xu, Methazolamide Calcium Phosphate Nanoparticles in an Ocular Delivery System, YAKUGAKU ZASSHI 130 (2010) 419–424, https://doi.org/10.1248/yakushi.130.419.

[13] J. Sun, Y. Lei, Z. Dai, X. Liu, T. Huang, J. Wu, Z.P. Xu, X. Sun, Sustained Release of Brimonidine from a New Composite Drug Delivery System for Treatment of Glaucoma, ACS Appl. Mater. Interfaces 9 (2017) 7990–7999, https://doi.org/10.1021/acsami.6b16509.

[14] S.E.-S. Radwan, R.M. El-Moslemany, R.A. Mehanna, E.H. Thabet, E.-Z. A. Abdelfattah, A. El-Kamel, Chitosan-coated bovine serum albumin nanoparticles for topical tetrandrine delivery in glaucoma: *in vitro* and *in vivo* assessment, Drug. Deliv. 29 (2022) 1150–1163, https://doi.org/10.1080/10717544.2022.2058648.

[15] V. Mishra, N.K. Jain, Acetazolamide encapsulated dendritic nano-architectures for effective glaucoma management in rabbits, Int. J. Pharm. 461 (2014) 380–390, https://doi.org/10.1016/j.ijpharm.2013.11.043.

[16] S. Gupta, Carbopol/Chitosan Based pH Triggered In Situ Gelling System for Ocular Delivery of Timolol Maleate, Sci. Pharm. 78 (2010) 959–976, https://doi.org/10.3797/scipharm.1001-06.

[17] O. Cegielska, P. Sajkiewicz, Targeted Drug Delivery Systems for the Treatment of Glaucoma: Most Advanced Systems Review, Polymers 11 (2019) 1742, https://doi.org/10.3390/polym11111742.

[18] R. Ilka, M. Mohseni, M. Kianirad, M. Naseripour, K. Ashtari, B. Mehravi, Nanogel-based natural polymers as smart carriers for the controlled delivery of Timolol Maleate through the cornea for glaucoma, Int. J. Biol. Macromol. 109 (2018) 955–962, https://doi.org/10.1016/j.ijbiomac.2017.11.090.

[19] E.V. Shimanovskaya, I.I. Nikol'skaya, P.V. Binevskii, O.V. Beznos, N.L. Klyachko, T.A. Pavlenko, N.B. Chesnokova, O.A. Kost, Lisinopril in the composition of calcium phosphate nanoparticles as a promising antiglaucoma agent, Nanotechnol. Russ. 9 (2014) 219–226, https://doi.org/10.1134/S1995078014020141.

[20] E.V. Shimanovskaia, O.V. Beznos, N.L. Kliachko, O.A. Kost, I.I. Nikol'skaia, T. A. Pavlenko, N.B. Chesnokova, A.V. Kabanov, [Production of timolol containing calcium-phosphate nanoparticles and evaluation of their effect on intraocular pressure in experiment], Vestn. Oftalmol. 128 (2012) 15–18.

[21] O.V. Beznos, V.E. Tikhomirova, E.V. Popova, T.A. Pavlenko, O.A. Kost, N. B. Chesnokova, Calcium-Phosphate Nanoparticles — a System for Drug Delivery to the Anterior Eye Chamber, Oftal'mologiâ 18 (2021) 331–337, https://doi.org/10.18008/1816-5095-2021-2-331-337.

[22] E. Popova, V. Tikhomirova, O. Beznos, N. Chesnokova, Y. Grigoriev, M. Taliansky, O. Kost, A Direct Comparison of Peptide Drug Delivery Systems Based on the Use of Hybrid Calcium Phosphate/Chitosan Nanoparticles versus Unmixed Calcium Phosphate or Chitosan Nanoparticles In Vitro and In Vivo, IJMS 24 (2023) 15532, https://doi.org/10.3390/ijms242115532.

[23] I.I. Nikolskaya, O.V. Beznos, A.I. Eltsov, I.V. Gachok, N.B. Chesnokova, V. P. Varlamov, O.A. Kost, The Inclusion of Timolol and Lisinopril in Calcium Phosphate Particles Covered by Chitosan: Application in Ophthalmology, Mosc. Univ. Chem. Bull. 73 (2018) 85–89, https://doi.org/10.3103/S0027131418020116.

[24] P.V. Binevski, N.G. Balabushevich, V.I. Uvarova, A.S. Vikulina, D. Volodkin, Bio-friendly encapsulation of superoxide dismutase into vaterite CaCO3 crystals. Enzyme activity, release mechanism, and perspectives for ophthalmology, Colloids Surf. B Biointerfaces 181 (2019) 437–449, https://doi.org/10.1016/j.colsurfb.2019.05.077.

[25] D.B. Trushina, T.N. Borodina, S. Belyakov, M.N. Antipina, Calcium carbonate vaterite particles for drug delivery: Advances and challenges, Mater. Today Adv. 14 (2022) 100214, https://doi.org/10.1016/j.mtadv.2022.100214.

[26] Y.I. Svenskaya, H. Fattah, O.A. Inozemtseva, A.G. Ivanova, S.N. Shtykov, D. A. Gorin, B.V. Parakhonskiy, Key Parameters for Size- and Shape-Controlled Synthesis of Vaterite Particles, Cryst. Growth & Des. 18 (2018) 331–337, https://doi.org/10.1021/acs.cgd.7b01328.

[27] A. Vikulina, J. Webster, D. Voronin, E. Ivanov, R. Fakhrullin, V. Vinokurov, D. Volodkin, Mesoporous additive-free vaterite CaCO3 crystals of untypical sizes: From submicron to Giant, Mater. & Des. 197 (2021) 109220, https://doi.org/10.1016/j.matdes.2020.109220.

[28] N.G. Balabushevich, E.A. Kovalenko, E.V. Mikhalchik, L.Y. Filatova, D. Volodkin, A.S. Vikulina, Mucin adsorption on vaterite CaCO3 microcrystals for the prediction of mucoadhesive properties, J. Colloid Interface Sci. 545 (2019) 330–339, https://doi.org/10.1016/j.jcis.2019.03.042.

[29] FDA, Angiotensin-Converting Enzyme Inhibitor (ACE Inhibitor) Drugs. https://www.fda.gov/drugs/postmarket-drug-safety-information-patients-and-providers/angiotensin-converting-enzyme-inhibitor-ace-inhibitor-drugs, in: n.d. https://www.fda.gov/drugs/postmarket-drug-safety-information-patients-and-providers/angiotensin-converting-enzyme-inhibitor-ace-inhibitor-drugs..

[30] N.B. Chesnokova, O.A. Kost, I.I. Nikolskaya, O.V. Beznos, N.G. Davydova, E.P. Stolyarova, P.V. Binevsky, T.A. PavlenkoThe impact of topical application of angiotensin-converting enzyme inhibitors on intraocular pressure, eye hydrodynamics and the activity of angiotensin-converting enzyme in the tear and aqueous humor. An experimental study, 2 (n.d.) 42–48..

[31] R. Agarwal, A.V. Krasilnikova, I.S. Raja, P. Agarwal, N. Mohd Ismail, Mechanisms of angiotensin converting enzyme inhibitor-induced IOP reduction in normotensive rats, Eur. J. Pharmacol. 730 (2014) 8–13, https://doi.org/10.1016/j.ejphar.2014.02.021.

[32] G.B. Shah, S. Sharma, A.A. Mehta, R.K. Goyal, Oculohypotensive Effect of Angiotensin-Converting Enzyme Inhibitors in Acute and Chronic Models of Glaucoma, J. Cardiovasc. Pharmacol. 36 (2000) 169–175, https://doi.org/10.1097/00005344-200008000-00005.

[33] O.A. Kost, N.V. Bovin, E.E. Chemodanova, V.V. Nasonov, T.A. Orth, New feature of angiotensin-converting enzyme: carbohydrate-recognizing domain, J. Mol. Recognit. 13 (2000) 360–369, https://doi.org/10.1002/1099-1352(200011/12)13:6%253C360:AID-JMR508%253E3.0.CO;2-K.

[34] D.V. Volodkin, A.I. Petrov, M. Prevot, G.B. Sukhorukov, Matrix Polyelectrolyte Microcapsules: New System for Macromolecule Encapsulation, Langmuir 20 (2004) 3398–3406, https://doi.org/10.1021/la036177z.

[35] D.B. Trushina, T.V. Bukreeva, M.N. Antipina, Size-Controlled Synthesis of Vaterite Calcium Carbonate by the Mixing Method: Aiming for Nanosized Particles, Cryst. Growth & Des. 16 (2016) 1311–1319, https://doi.org/10.1021/acs.cgd.5b01422.

[36] S.V. German, M.V. Novoselova, D.N. Bratashov, P.A. Demina, V.S. Atkin, D. V. Voronin, B.N. Khlebtsov, B.V. Parakhonskiy, G.B. Sukhorukov, D.A. Gorin, High-efficiency freezing-induced loading of inorganic nanoparticles and proteins into micron- and submicron-sized porous particles, Sci. Rep. 8 (2018) 17763, https://doi.org/10.1038/s41598-018-35846-x.

[37] A.I. Petrov, D.V. Volodkin, G.B. Sukhorukov, Protein-Calcium Carbonate Coprecipitation: A Tool for Protein Encapsulation, Biotechnol. Progress. 21 (2008) 918–925, https://doi.org/10.1021/bp0495825.

[38] S.M. Danilov, I.V. Balyasnikova, R.F. Albrecht, O.A. Kost, Simultaneous Determination of ACE Activity with 2 Substrates Provides Information on the Status of Somatic ACE and Allows Detection of Inhibitors in Human Blood, J. Cardiovasc. Pharmacol. 52 (2008) 90–103, https://doi.org/10.1097/FJC.0b013e31817fd3bc.

[39] A. Afanasiev, H. Yao, C. Marcheselli, I. Lahdesmaki, B.A. Parviz, A synthetic eye platform for testing contact lenses with integrated electronic biosensors, in: in: 2011 11th IEEE International Conference on Nanotechnology, IEEE, Portland, OR, USA, 2011, pp. 358–361, https://doi.org/10.1109/NANO.2011.6144612.

[40] DrugBank Online. DrugBank Salt Summary for DBSALT002434, Enalaprilat: dehydrate; https://go.drugbank.com/salts/DBSALT002434, in: n.d. https://go.drugbank.com/salts/DBSALT002434..

[41] O. Svensson, K. Thuresson, T. Arnebrant, Interactions between chitosan-modified particles and mucin-coated surfaces, J. Colloid Interface Sci. 325 (2008) 346–350, https://doi.org/10.1016/j.jcis.2008.06.013.

[42] H. Li, F. Dai, H. Liu, Q. Tao, J. Hu, Y. Zhang, Z. Xiao, I.D. Rupenthal, H. Li, F. Yang, W. Li, H. Lin, D. Hou, Physicochemical properties and micro-interaction between micro-nanoparticles and anterior corneal multilayer biological interface film for improving drug delivery efficacy: the transformation of tear film turnover mode, Drug. Deliv. 30 (2023) 2184312, https://doi.org/10.1080/10717544.2023.2184312.

[43] A. Daerr, A. Mogne, Pendent_Drop: An ImageJ Plugin to Measure the Surface Tension from an Image of a Pendent Drop, JORS 4 (2016) 3, https://doi.org/10.5334/jors.97.

[44] A.R. Mackie, F.M. Goycoolea, B. Menchicchi, C.M. Caramella, F. Saporito, S. Lee, K. Stephansen, I.S. Chronakis, M. Hiorth, M. Adamczak, M. Waldner, H.M. Nielsen, L. Marcelloni, Innovative Methods and Applications in Mucoadhesion Research, Macromol. Biosci. 17 (2017) 1600534, https://doi.org/10.1002/mabi.201600534.

[45] Y.B. Choy, J.-H. Park, M.R. Prausnitz, Mucoadhesive microparticles engineered for ophthalmic drug delivery, J. Phys. Chem. Solids 69 (2008) 1533–1536, https://doi.org/10.1016/j.jpcs.2007.10.043.

[46] H. Li, X. Zhang, X. Lin, S. Zhuang, Y. Wu, Z. Liu, J. Rong, J. Zhao, $CaCO_3$ nanoparticles pH-sensitively induce blood coagulation as a potential strategy for starving tumor therapy, J. Mater. Chem. B 8 (2020) 1223–1234, https://doi.org/10.1039/C9TB02684C.

[47] R.V. Moiseev, D.B. Kaldybekov, S.K. Filippov, A. Radulescu, V.V. Khutoryanskiy, Maleimide-Decorated PEGylated Mucoadhesive Liposomes for Ocular Drug Delivery, Langmuir 38 (2022) 13870–13879, https://doi.org/10.1021/acs.langmuir.2c02086.

[48] Z. Huang, R.V. Moiseev, S.S. Melides, W. Bae, I. Jurewicz, V.V. Khutoryanskiy, J. L. Keddie, Pickering emulsions stabilised with oligoglycine-functionalised nanodiamond as a model system for ocular drug delivery applications, Soft Matter 19 (2023) 5513–5526, https://doi.org/10.1039/D3SM00495C.

[49] N.J. Van Haeringen, Clinical biochemistry of tears, Surv. Ophthalmol. 26 (1981) 84–96, https://doi.org/10.1016/0039-6257(81)90145-4.

[50] J.M. Tiffany, The Normal Tear Film, in: G. Geerling, H. Brewitt (Eds.), Developments in Ophthalmology, KARGER, Basel, 2008, pp. 1–20, https://doi.org/10.1159/000131066.

[51] R. Barnett, S. Aronson, A biomicroscopic method for quantitation of ocular and adnexal toxicity, Fundam. Appl. Toxicol. 3 (1983) 187–191, https://doi.org/10.1016/S0272-0590(83)80080-3.

[52] M. Mihai, S. Racovita, A.-L. Vasiliu, F. Doroftei, C. Barbu-Mic, S. Schwarz, C. Steinbach, F. Simon, Autotemplate Microcapsules of $CaCO_3$ /Pectin and Nonstoichiometric Complexes as Sustained Tetracycline Hydrochloride Delivery Carriers, ACS Appl. Mater. Interfaces 9 (2017) 37264–37278, https://doi.org/10.1021/acsami.7b09333.

[53] S. Racovita, A.-L. Vasiliu, A. Bele, D. Schwarz, C. Steinbach, R. Boldt, S. Schwarz, M. Mihai, Complex calcium carbonate/polymer microparticles as carriers for aminoglycoside antibiotics, RSC Adv. 8 (2018) 23274–23283, https://doi.org/10.1039/C8RA03367F.

[54] D. Ding, B. Kundukad, A. Somasundar, S. Vijayan, S.A. Khan, P.S. Doyle, Design of Mucoadhesive PLGA Microparticles for Ocular Drug Delivery, ACS Appl. Bio Mater. 1 (2018) 561–571, https://doi.org/10.1021/acsabm.8b00041.

[55] M. Hotujac Grgurević, M. Juretić, A. Hafner, J. Lovrić, I. Pepić, Tear fluid-eye drops compatibility assessment using surface tension, Drug. Dev. Ind. Pharm. 43 (2017) 275–282, https://doi.org/10.1080/03639045.2016.1238924.

[56] T. Bíró, G. Horvát, M. Budai-Szűcs, E. Csányi, E. Urbán, A. Facskó, P. Szabó-Révész, I. Csóka, Z. Aigner, Development of prednisolone-containing eye drop formulations by cyclodextrin complexation and antimicrobial, mucoadhesive biopolymer, DDDT 12 (2018) 2529–2537, https://doi.org/10.2147/DDDT.S165693.

[57] K. Han, O.E. Woghiren, R. Priefer, Surface tension examination of various liquid oral, nasal, and ophthalmic dosage forms, Chem. Cent. J. 10 (2016) 31, https://doi.org/10.1186/s13065-016-0176-x.

[58] W. He, X. Huang, J. Zhang, Y. Zhu, Y. Liu, B. Liu, Q. Wang, X. Huang, D. He, CaCO3–Chitosan Composites Granules for Instant Hemostasis and Wound Healing, Materials 14 (2021) 3350, https://doi.org/10.3390/ma14123350.
[59] M.Y. Memar, K. Adibkia, S. Farajnia, H.S. Kafil, S. Maleki Dizaj, R. Ghotaslou, Biocompatibility, cytotoxicity and antimicrobial effects of gentamicin-loaded CaCO3 as a drug delivery to osteomyelitis, J. Drug. Deliv. Sci. Technol. 54 (2019) 101307, https://doi.org/10.1016/j.jddst.2019.101307.
[60] Y. Sultana, R. Jain, M. Aqil, A. Ali, Review of Ocular Drug Delivery, CDD 3 (2006) 207–217, https://doi.org/10.2174/156720106776359186.
[61] A. Zimmer, J. Kreuter, Microspheres and nanoparticles used in ocular delivery systems, Adv. Drug. Deliv. Rev. 16 (1995) 61–73, https://doi.org/10.1016/0169-409X(95)00017-2.
[62] K. Tsubota, Y. Monden, Y. Yagi, E. Goto, S. Shimmura, New treatment of dry eye: the effect of calcium ointment through eyelid skin delivery, Br. J. Ophthalmol. 83 (1999) 767–770, https://doi.org/10.1136/bjo.83.7.767.